Geophysical Journal International

Geophys. J. Int. (2025) **243,** 1–18
Advance Access publication 2025 September 25
Research Paper

https://doi.org/10.1093/gji/ggaf381

A novel fast sweeping method for computing the attenuation operator t^* in absorbing media

Dongdong Wang,[1] Jing Chen,[1] Shijie Hao[1] and Ping Tong[1,2,3]

[1] *Division of Mathematical Sciences, School of Physical and Mathematical Sciences, Nanyang Technological University, Singapore 637371, Singapore. E-mail: tongping@ntu.edu.sg*
[2] *Earth Observatory of Singapore, Nanyang Technological University, Singapore 639798, Singapore*
[3] *Asian School of the Environment, Nanyang Technological University, Singapore 639798, Singapore*

Accepted 2025 September 22. Received 2025 August 26; in original form 2025 January 10

SUMMARY

The attenuation operator t^* represents the total path attenuation and characterizes the amplitude decay of a propagating seismic wave. Calculating t^* is typically required in seismic attenuation tomography. Traditional methods for calculating t^* require determining the ray path explicitly. However, ray tracing can be computationally intensive when processing large data sets, and conventional ray tracing techniques may fail even in mildly heterogeneous media. In this study, we propose a modified fast sweeping method (MFSM) to solve the governing equation for t^* without explicitly calculating the ray path. The approach consists of two main steps. First, the traveltime field is calculated by numerically solving the eikonal equation using the fast sweeping method. Secondly, t^* is computed by solving its governing equation with the MFSM, based on the discretization of the gradient of t^* using an upwinding scheme derived from the traveltime gradient. The MFSM is rigorously validated through comparisons with analytical solutions and by examining t^* errors under grid refinement in both simple and complex models. Key performance metrics, including convergence, number of iterations and computation time, are evaluated. Two versions of the MFSM are developed for both Cartesian and spherical coordinate systems. We demonstrate the practical applicability of the developed MFSM in calculating t^* in North Island, and discuss the method's efficiency in estimating earthquake response spectra.

Key words: Numerical modelling; Seismic attenuation; Wave propagation.

1 INTRODUCTION

Seismic attenuation, apart from geometrical spreading, is the primary process that reduces the amplitude and modifies the phase of a propagating seismic wave. Attenuation is quantified by the quality factor, Q, defined as the ratio of energy lost during a wave cycle to the total energy of the cycle. The reciprocal of Q, denoted as $1/Q$, depends on the rock properties and accounts for energy loss through elastic and anelastic mechanisms, referred to as scattering and intrinsic attenuation, respectively (Sato *et al.* 2012). Scattering attenuation arises from the interaction of seismic waves with small-scale heterogeneities in the elastic properties of the medium, such as those caused by intense rock fracturing. On the other hand, intrinsic attenuation occurs when the kinetic energy of seismic waves is converted into thermal energy, either through internal friction along cracks or via viscoelastic deformation of the medium. In practical applications, with separation of seismic scattering from absorption, the inversion yields intrinsic Q; without separation, the inversion yields total Q.

A widely used method for determining Q is based on the estimation of the attenuation operator t^*, which accounts for the damping of the wave amplitude A through the exponential decay $e^{-\omega t^*/2}$ (e.g. Cormier 1982; Bindi *et al.* 2006), where ω is the angular frequency. Physically, t^* represents the cumulative attenuation along a ray path connecting the hypocentre to the station (Kanamori 1967). It can be mathematically defined as $t^* = \int_L 1/(V(\boldsymbol{x})Q(\boldsymbol{x}))dl$, where $V(\boldsymbol{x})$ and $Q(\boldsymbol{x})$ are the seismic wave velocity and quality factor, respectively, L is the ray path. Synthetic t^* values are typically calculated by summation along the ray path (e.g. Lees & Lindley 1994; Eberhart-Phillips *et al.* 2008; De Siena *et al.* 2009). Consequently, the accuracy of t^* is heavily dependent on the accuracy of the ray path. Over the past few decades, a variety of seismic ray tracing techniques have been developed to determine ray paths. These include shooting and bending ray tracing methods, as well as numerical solutions to the eikonal equation on a grid. Specifically, shooting methods treat the ray equation as an initial value problem, iteratively adjusting the ray's take-off angle until the source–receiver path is found (e.g. Červený 1987; Sambridge 1990; Rawlinson *et al.* 2001).

Bending methods (e.g. Julian & Gubbins 1977; Um & Thurber 1987) iteratively modify the geometry of an initially assumed path between the source and receiver until it conforms to the Fermat's principle. The pseudo-bending technique (Um & Thurber 1987) and the thurber-modified ray-bending approach (Block 1991), have been widely used to trace ray paths in attenuation tomography (e.g. Lees & Lindley 1994; Eberhart-Phillips *et al.* 2008; De Siena *et al.* 2009, 2010, 2014; Prudencio *et al.* 2015a; Wei & Wiens 2018; Sketsiou *et al.* 2021).

However, both shooting and bending methods may fail to converge on the true ray paths in the presence of velocity variations (e.g. Rawlinson & Sambridge 2004). This issue becomes increasingly pronounced as the complexity of the medium grows. Recently, grid-based schemes, such as the fast marching method (FMM) (e.g. Sethian 1996; Sethian & Popovici 1999; Alkhalifah & Fomel 2001) and the fast sweeping method (FSM) (e.g. Zhao 2005; Qian *et al.* 2007; Luo & Qian 2012), have gained significant popularity. These methods numerically solve the eikonal equation on a gridded velocity field to compute the traveltime from the source to every grid point. The ray path is then traced from the receiver to the source along the negative gradient of the traveltime field. These approaches are fast, accurate and robust for calculating traveltime fields, even in complex heterogeneous media (Rawlinson *et al.* 2010). Theoretically, grid-based methods can provide relatively accurate ray paths, enabling the summation along these paths to yield a more precise estimation of t^*.

The aforementioned studies focus on methods for calculating t^* that rely on ray tracing. However, ray tracing can be computationally expensive, particularly when dealing with a large number of sources and/or receivers in a 3-D medium (Rawlinson & Sambridge 2004). In addition, the development of the adjoint-state attenuation tomography method requires the calculation of t^* without the use of ray tracing (e.g. He 2020; Huang *et al.* 2020). To address this issue and take advantages of grid-based methods, a grid-based approach for calculating t^* needs to be developed. By converting the integral form of t^* to its differential form and considering the relationship between the gradient and the directional derivative, Huang *et al.* (2020) derive the governing equation for t^*. Later, He (2022) reformulates the governing equation for t^* using the Leibniz formula and develops a parallel FSM to solve it. However, their study would benefit from further verification and evaluation, as well as a more in-depth analysis of accuracy and convergence, and is primarily focused on solving the equation in Cartesian coordinates.

In this paper, we develop a modified fast sweeping method (MFSM) as an alternative approach for solving the t^* governing equation. Considering that t^* accumulates along the ray path, which is not directly determined by traveltime but rather by the traveltime gradient, the calculation of t^* thus depends on the traveltime gradient. The traveltime field is first calculated using the FSM, after which t^* is determined by the MFSM through an upwinding scheme derived from the traveltime gradient. Our proposed MFSM provides an effective and accurate method for calculating t^* without the need for ray tracing and serves as a promising forward modelling tool for adjoint-state attenuation tomography.

The paper is organized as follows. From the definition of t^*, we provide a complete derivation of the governing equation for t^* in differential form in Section 2.1. Then, the FSM for solving the eikonal equation is reviewed in Section 2.2, and the MFSM for solving the t^* governing equation is introduced in Section 2.3. In Section 3, considering several simple and complex models, we verify the MFSM by comparing its solutions with the analytical solutions and analyse the relative and absolute t^* errors with grid refinement. The convergence analysis, number of iterations and computational time are presented in Section 4. In Section 5, we consider realistic velocity and attenuation models for North New Zealand region and apply the MFSM to calculate and analyse the t^* field. Finally, we discuss and summarize the results in Section 6.

2 GOVERNING EQUATIONS AND NUMERICAL ALGORITHMS

2.1 Governing equation for the attenuation operator t^*

We denote the propagation velocity of the wave under consideration (either P or S) by $V(\boldsymbol{x})$. The traveltime t from the source to the receiver can be calculated by integrating the reciprocal of the velocity along the ray path connecting them (Červený 2001)

$$t = \int_L \frac{1}{V(\boldsymbol{x})} \mathrm{d}l, \tag{1}$$

where $\mathrm{d}l$ is the arc length along the ray path L. In viscoelastic media, the reciprocal of the quality factor, $1/Q$, is commonly used to quantify attenuation. A high Q indicates low attenuation, while a low Q indicates high attenuation. Previous studies suggest that attenuation primarily affects the waveform through the complex and frequency-dependent traveltime, rather than considerably altering ray paths, provided that $1/Q \ll 1$ (Keers *et al.* 2001). The attenuation operator t^* can be expressed as (e.g. Stachnik *et al.* 2004; Wei & Wiens 2018)

$$t^* = \int_L \frac{1}{V(\boldsymbol{x})Q(\boldsymbol{x})} \mathrm{d}l, \tag{2}$$

where $Q(\boldsymbol{x})$ represents the P-wave or S-wave quality factor. It is worth noting that, in the special case where $V(\boldsymbol{x})Q(\boldsymbol{x}) = 1$, the numerical calculation of eq. (2) was previously addressed by Cohen & Kimmel (1997), Deschamps & Cohen (2001) and Cohen (2006) in the context of calculating the Euclidean length of minimal paths. The integral eqs (1) and (2) can be rewritten in differential forms as,

$$\frac{\mathrm{d}t}{\mathrm{d}l} = \frac{1}{V(\boldsymbol{x})}, \tag{3}$$

$$\frac{\mathrm{d}t^*}{\mathrm{d}l} = \frac{1}{V(\boldsymbol{x})Q(\boldsymbol{x})}, \tag{4}$$

where both $\mathrm{d}t/\mathrm{d}l$ and $\mathrm{d}t^*/\mathrm{d}l$ represent the directional derivatives along the ray paths. Mathematically, these two differentials can be expressed as:

$$\frac{\mathrm{d}t}{\mathrm{d}l} = \nabla t(\boldsymbol{x}) \cdot \frac{\boldsymbol{l}}{|\boldsymbol{l}|}, \tag{5}$$

$$\frac{\mathrm{d}t^*}{\mathrm{d}l} = \nabla t^*(\boldsymbol{x}) \cdot \frac{\boldsymbol{l}}{|\boldsymbol{l}|}, \tag{6}$$

where $\boldsymbol{l}/|\boldsymbol{l}|$ denotes the unit tangent vector along the ray path direction, and ∇t and ∇t^* represent the gradients of t and t^*, respectively. Notably, the same unit vector $\boldsymbol{l}/|\boldsymbol{l}|$ appearing in eqs (5) and (6) indicates the identical evolution direction for both t and t^*. In an isotropic medium, $\boldsymbol{l}/|\boldsymbol{l}|$ is equivalent to the unit normal of the wave front:

$$\frac{\boldsymbol{l}}{|\boldsymbol{l}|} = \frac{\nabla t(\boldsymbol{x})}{|\nabla t(\boldsymbol{x})|}. \tag{7}$$

For simplicity, in the following derivation we use $s(\boldsymbol{x})$ (slowness) to represent $1/V(\boldsymbol{x})$ and $q(\boldsymbol{x})$ to represent $1/Q(\boldsymbol{x})$. Based on eqs (3), (5), (7), the eikonal equation governing wave front propagation from the point source $\boldsymbol{x}_s$ to any position $\boldsymbol{x}$, with a zero boundary condition at $\boldsymbol{x}_s$, can be expressed as

$$\nabla t(\boldsymbol{x}) \cdot \nabla t(\boldsymbol{x}) = s^2(\boldsymbol{x}), \quad t(\boldsymbol{x}_s) = 0. \tag{8}$$

It is important to note that under the high-frequency approximation, eq. (8) can also be derived from the wave equation (Shearer 2019). Similarly, combining eqs (4), (6), (7) and (8), we can obtain

$$\nabla t(\boldsymbol{x}) \cdot \nabla t^*(\boldsymbol{x}) = q(\boldsymbol{x}) s^2(\boldsymbol{x}), \quad t^*(\boldsymbol{x}_s) = 0. \tag{9}$$

Thus, we have established eq. (9) as the governing equation for t^* in attenuation media. The derivation of eq. (9) follows a similar workflow to that presented in Huang *et al.* (2020), but we provide a more detailed procedure here. One difference is that, unlike eq. (1), in Huang *et al.* (2020), t^* is defined as $t^* = \int_L \pi/(V(\boldsymbol{x})Q(\boldsymbol{x}))\mathrm{d}l$. Thus, the constant π is absent from the right-hand side of eq. (9) compared with that in Huang *et al.* (2020). Both types of t^* governing equation are practical, as we can choose to include the constant π in the governing equation for t^*, or incorporate it when measuring the observed t^*.

It should be mentioned that solving eq. (9) is mathematically equivalent to differentiating the solution of the eikonal equation with respect to the metric—a concept early introduced in Benmansour *et al.* (2010) along with a proposed fast-marching-like numerical method. This approach was further developed in Mirebeau & Dreo (2017), which extended it to anisotropic metrics, and in Bertrand *et al.* (2023), which applied it in the context of neural network architectures. In the following, we introduce an alternative numerical method, the fast sweeping method (FSM) to solve eq. (9).

2.2 Overview of the FSM for solving the eikonal eq. (8)

To compute $t^*(\boldsymbol{x})$ using eq. (9), it is first necessary to determine the traveltime field $t(\boldsymbol{x})$ by solving eq. (8). In this study, we use the FSM, an iterative algorithm, to solve eq. (8) on a rectangular grid to obtain the traveltime field $t(\boldsymbol{x})$ (Zhao 2005). Other numerical methods (e.g. the fast marching method (FMM) (e.g. Sethian 1996; Sethian & Popovici 1999; Alkhalifah & Fomel 2001) and the fast iterative method (FIM) (e.g. Jeong & Whitaker 2008)) can also be used to calculate $t(\boldsymbol{x})$, since the calculations of $t(\boldsymbol{x})$ and $t^*(\boldsymbol{x})$ are decoupled. Below, we provide a brief overview of the FSM for solving eq. (8). The core idea of the FSM is the utilization of nonlinear upwind differences combined with Gauss–Seidel iterations, executed in alternating sweeping orders. This method is straightforward to implement and highly efficient for parallel computation.

We present the algorithm for solving eq. (8) in 3-D Cartesian coordinates (Zhao 2005). To address applications on a global scale, we also extend the algorithm to spherical coordinates, as detailed in Appendix A. In 3-D Cartesian coordinates ($\boldsymbol{x} = (x, y, z)$), the gradient operator is expressed as $\nabla t(\boldsymbol{x}) = (\partial_x t, \partial_y t, \partial_z t)$. First, the 3-D domain $\Omega \subset \mathcal{R}^3$ is discretized into a uniform mesh of grid points $\boldsymbol{x}_{i,j,k}$ with grid spacings Δx, Δy and Δz. The total number of grid points in the x, y and z directions are M_I, M_J and M_K. Employing the Godunov upwind difference scheme to discretize eq. (8) at interior grid points ($2 \le i \le M_I - 1, 2 \le j \le M_J - 1, 2 \le k \le M_K - 1$), we obtain

$$\left[\frac{(t_{i,j,k} - t^{x\,\min}_{i,j,k})^+}{\Delta x}\right]^2 + \left[\frac{(t_{i,j,k} - t^{y\,\min}_{i,j,k})^+}{\Delta y}\right]^2 + \left[\frac{(t_{i,j,k} - t^{z\,\min}_{i,j,k})^+}{\Delta z}\right]^2 = s^2_{i,j,k}, \tag{10}$$

where

$$t^{x\,\min}_{i,j,k} = \min(t_{i-1,j,k}, t_{i+1,j,k}), \quad t^{y\,\min}_{i,j,k} = \min(t_{i,j-1,k}, t_{i,j+1,k}), \quad t^{z\,\min}_{i,j,k} = \min(t_{i,j,k-1}, t_{i,j,k+1}), \tag{11}$$

and

$$(x)^+ = \begin{cases} x, & x > 0, \\ 0, & x \le 0. \end{cases} \tag{12}$$

At the boundaries of the region (i.e. $i = 1 \vee M_I$; $j = 1 \vee M_J$; $k = 1 \vee M_K$), one-sided difference schemes are applied. For instance, at the left boundary $\boldsymbol{x}_{1,j,k}$, the use of a one-sided difference yields

$$\left[\frac{(t_{1,j,k} - t_{2,j,k})^+}{\Delta x}\right]^2 + \left[\frac{(t_{1,j,k} - t^{y\,\min}_{1,j,k})^+}{\Delta y}\right]^2 + \left[\frac{(t_{1,j,k} - t^{z\,\min}_{1,j,k})^+}{\Delta z}\right]^2 = s^2_{1,j,k}, \tag{13}$$

Subsequently, the traveltime field $t(\boldsymbol{x})$ can be determined using the Fast Sweeping Algorithm (e.g. Zhao 2005; Leung & Qian 2006; Fomel *et al.* 2009), together with solving of eqs (10) and (13). The sweeping order of the Fast Sweeping Algorithm in 2-D Cartesian coordinates is illustrated in Figs 1(a)–(d). Algorithm 1 details the steps of the Fast Sweeping Algorithm.

Algorithm 1 Fast sweeping algorithm – 3-D local solver

```
Initialize:
n = 1
for all grid points (i, j, k) do
    if x_{i,j,k} = x_s (Source location) then
        t^1_{i,j,k} ← 0
    else
        t^1_{i,j,k} ← ∞ or a sufficiently large number
    end if
end for
repeat
    Gauss-Seidel Iterations: Perform sweeps in 8 alternating directions.
    Define the sweeping index ranges:
    (1) i = 1 : M_I, j = 1 : M_J, k = 1 : M_K      (2) i = M_I : 1, j = 1 : M_J, k = 1 : M_K
    (3) i = 1 : M_I, j = M_J : 1, k = 1 : M_K      (4) i = M_I : 1, j = M_J : 1, k = 1 : M_K
    (5) i = 1 : M_I, j = 1 : M_J, k = M_K : 1      (6) i = M_I : 1, j = 1 : M_J, k = M_K : 1
    (7) i = 1 : M_I, j = M_J : 1, k = M_K : 1      (8) i = M_I : 1, j = M_J : 1, k = M_K : 1
    for each sweep direction do
        for i in i-range do
            for j in j-range do
                for k in k-range do
                    Compute t̂^{n+1}_{i,j,k} using t^n_{i±1,j,k}, t^n_{i,j±1,k}, and t^n_{i,j,k±1}
                    according to eqs (10) and (13)
                    t^{n+1}_{i,j,k} ← min(t^n_{i,j,k}, t̂^{n+1}_{i,j,k})
                end for
            end for
        end for
    end for
    n ← n + 1
until ||t^{(n+1)} − t^{(n)}||_{L^1} ≤ ε
```

2.3 Modified FSM for solving the t^* governing eq. (9)

In this section, we present a method for solving eq. (9) using the well-determined $t(\boldsymbol{x})$, along with the velocity and attenuation models, to

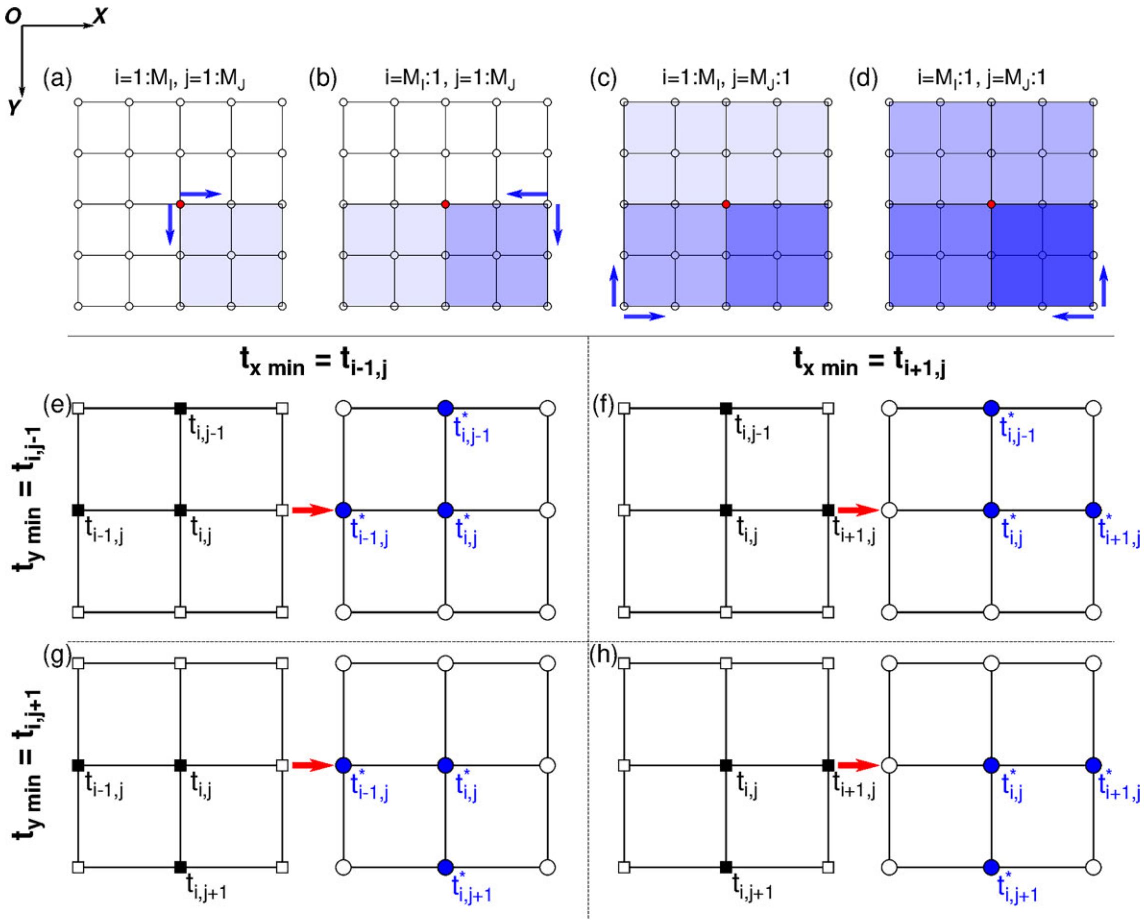

Figure 1. Illustration of the sweeping order in the fast sweeping algorithm and the discretization of partial derivatives of t^* using the upwind difference scheme for t in Cartesian coordinates. In (a), (b), (c) and (d), the blue arrows represent the sweeping directions, starting respectively from the upper-left, upper-right, lower-left and lower-right corners of the computational domain. The red circle marks the source location. Grid nodes within the white area represent their t (or t^*) values are yet to be updated, while grid nodes in the blue area indicate their t (or t^*) values have already been updated. Darker shades of blue signify more recent updates. (e), (f), (g) and (h) display four conditions for selecting grids to discretize the partial derivatives of t^* using the upwind difference scheme for t. Black squares denote traveltime t, while blue circles represent t^*.

compute $t^*(\boldsymbol{x})$. To achieve this, we propose a MFSM to calculate $t^*(\boldsymbol{x})$ based on $t(\boldsymbol{x})$ and its gradient.

In 3-D Cartesian coordinates, we discretize eq. (9) at the interior grid points ($2 \le i \le M_I - 1, 2 \le j \le M_J - 1, 2 \le k \le M_K - 1$) into the following difference form:

$$\frac{\left(t_{i,j,k}-t^{x\min}_{i,j,k}\right)^+}{\Delta x}\frac{\left(t^*_{i,j,k}-t^{*,x\min}_{i,j,k}\right)}{\Delta x}+\frac{\left(t_{i,j,k}-t^{y\min}_{i,j,k}\right)^+}{\Delta y}\frac{\left(t^*_{i,j,k}-t^{*,y\min}_{i,j,k}\right)}{\Delta y}+\frac{\left(t_{i,j,k}-t^{z\min}_{i,j,k}\right)^+}{\Delta z}\frac{\left(t^*_{i,j,k}-t^{*,z\min}_{i,j,k}\right)}{\Delta z}=s^2_{i,j,k}q_{i,j,k}, \quad (14)$$

where $\nabla t(\boldsymbol{x})$ is discretized using the Godunov upwind difference scheme, as is done when solving the eikonal equation. Here, $t^{x\min}_{i,j,k}$, $t^{y\min}_{i,j,k}$ and $t^{z\min}_{i,j,k}$ are determined based on eq. (11). Since t^* accumulates in the same direction as t as the wave propagates outward, and the propagation direction depends on $\nabla t(\boldsymbol{x})$, the approximation of ∇t^* requires that the selection of $t^{*,x\min}_{i,j,k}$ aligns with the choice of $t^{x\min}_{i,j,k}$, as done when determining $\nabla t(\boldsymbol{x})$. Figs 1(e)–(h) illustrate how $t^{*,x\min}_{i,j}$ and $t^{*,y\min}_{i,j}$ are determined based on $t^{x\min}_{i,j}$ and $t^{y\min}_{i,j}$ in 2-D Cartesian coordinates. A similar strategy is applied in 3-D Cartesian coordinates. Mathematically, $t^{*,x\min}_{i,j,k}$, $t^{*,y\min}_{i,j,k}$ and $t^{*,z\min}_{i,j,k}$ can be determined using the following rulers:

$$t^{*,x\min}_{i,j,k} = \begin{cases} t^*_{i-1,j,k}, & \text{if } t^{x\min}_{i,j,k} = t_{i-1,j,k}, \\ t^*_{i+1,j,k}, & \text{if } t^{x\min}_{i,j,k} = t_{i+1,j,k}, \end{cases} \quad (15)$$

$$t^{*,y\min}_{i,j,k} = \begin{cases} t^*_{i,j-1,k}, & \text{if } t^{y\min}_{i,j,k} = t_{i,j-1,k}, \\ t^*_{i,j+1,k}, & \text{if } t^{y\min}_{i,j,k} = t_{i,j+1,k}, \end{cases} \quad (16)$$

$$t^{*,z\min}_{i,j,k} = \begin{cases} t^*_{i,j,k-1}, & \text{if } t^{z\min}_{i,j,k} = t_{i,j,k-1}, \\ t^*_{i,j,k+1}, & \text{if } t^{z\min}_{i,j,k} = t_{i,j,k+1}. \end{cases} \quad (17)$$

It should be noted that, similar to eq. (13), one-sided differences are employed at the boundaries of the computational domain. For instance, at the boundary point $\boldsymbol{x}_{1,j,k}$, we have

$$\frac{\left(t_{1,j,k}-t_{2,j,k}\right)^+}{\Delta x}\frac{\left(t^*_{1,j,k}-t^*_{2,j,k}\right)}{\Delta x}+\frac{\left(t_{1,j,k}-t^{y\min}_{1,j,k}\right)^+}{\Delta y}\frac{\left(t^*_{1,j,k}-t^{*,y\min}_{1,j,k}\right)}{\Delta y}+\frac{\left(t_{1,j,k}-t^{z\min}_{1,j,k}\right)^+}{\Delta z}\frac{\left(t^*_{1,j,k}-t^{*,z\min}_{1,j,k}\right)}{\Delta z}=s^2_{1,j,k}q_{1,j,k}. \quad (18)$$

Then, the $t^*(\boldsymbol{x})$ field can be determined using the modified Fast Sweeping Algorithm, together with solving of eqs (14) and (18).

Algorithm 2 Modified fast sweeping algorithm – 3-D local solver

Initialize:
$n = 1$
for all grid points (i, j, k) **do**
  if $\boldsymbol{x}_{i,j,k} = \boldsymbol{x}_s$ (Source location) **then**
    $t^{*1}_{i,j,k} \leftarrow 0$
  else
    $t^{*1}_{i,j,k} \leftarrow \infty$ or a sufficiently large number
  end if
end for
Note: The traveltime field $t(\boldsymbol{x})$ is fixed (not updated) during the following iterations.
repeat
  Gauss-Seidel Iterations: Perform sweeps in 8 alternating directions.
  Define the sweeping index ranges:
  (1) $i = 1 : M_I, j = 1 : M_J, k = 1 : M_K$ (2) $i = M_I : 1, j = 1 : M_J, k = 1 : M_K$
  (3) $i = 1 : M_I, j = M_J : 1, k = 1 : M_K$ (4) $i = M_I : 1, j = M_J : 1, k = 1 : M_K$
  (5) $i = 1 : M_I, j = 1 : M_J, k = M_K : 1$ (6) $i = M_I : 1, j = 1 : M_J, k = M_K : 1$
  (7) $i = 1 : M_I, j = M_J : 1, k = M_K : 1$ (8) $i = M_I : 1, j = M_J : 1, k = M_K : 1$
  for each sweep direction **do**
    for i in i-range **do**
      for j in j-range **do**
        for k in k-range **do**
          Compute $\widehat{t^*}^{n+1}_{i,j,k}$ using $t^n_{i\pm1,j,k}$, $t^n_{i,j\pm1,k}$, $t^n_{i,j,k\pm1}$, $t^{*n}_{i\pm1,j,k}$, $t^{*n}_{i,j\pm1,k}$, $t^{*n}_{i,j,k\pm1}$ according to eqs (14) and (18)
          $t^{*n+1}_{i,j,k} \leftarrow \min(t^{*n}_{i,j,k}, \widehat{t^*}^{n+1}_{i,j,k})$.
        end for
      end for
    end for
  end for
  $n \leftarrow n + 1$
until $\|t^{*(n+1)} - t^{*(n)}\|_{L^1} \leq \upsilon$

Algorithm 2 details the steps of the Modified Fast Sweeping Algorithm. Here, we should note that in heterogeneous media, the gradient $\nabla t(\boldsymbol{x})$ may be discontinuous, even though $t(\boldsymbol{x})$ itself remains continuous (Zhao 2005). As a result, $t^*(\boldsymbol{x})$ is in general discontinuous at points where there are several shortest paths. So, the convergence is not expected in the L^∞ norm. Instead, we use the L^1 norm as the convergence criteria. The discontinuity of $t^*(\boldsymbol{x})$ can be observed in the following numerical tests in Section 3.3. We have established the theoretical framework for the MFSM to determine t^* in Cartesian coordinates. The MFSM for determining t^* in spherical coordinates can be found in Appendix A.

3 VERIFICATION OF THE MFSM

In this section, we validate the MFSM by comparing it with analytical solutions and analyse its errors as the grid size is adjusted, considering several different models. All tests, algorithms and code presented are designed for the 3-D case, with $s(\boldsymbol{x})$ and $q(\boldsymbol{x})$ being homogeneous with respect to the $y-$axis. To avoid placing sources and receivers at the boundary while minimizing computational cost, we position them in the central $x - z$ plane, using three nodes along the $y-$axis.

3.1 Uniform velocity and attenuation model

We begin by considering Model 1, as shown in Figs 2(a) and (b), which is characterized by uniform V_P and Q_P in Cartesian coordinates. We first consider the region discretized with spatial intervals of $\Delta x = \Delta z = 0.20$ km, resulting in a grid of 151 by 151 grid nodes. For such uniform model, the analytical solutions for $t(\boldsymbol{x})$ and $t^*(\boldsymbol{x})$ can be easily derived. The $t(\boldsymbol{x})$ isolines computed using the FSM and their analytical solutions (Figs 2a and c), as well as $t^*(\boldsymbol{x})$ isolines calculated by the MFSM and their analytical solutions (Figs 2b and d), exhibit strong consistency. The pattern of $t^*(\boldsymbol{x})$ isolines closely resembles that of $t(\boldsymbol{x})$ isolines. However, the values represented by the isolines differ, with $t^*(\boldsymbol{x})$ being proportional to t by a factor of $1/500.0$, where 500.0 is the uniform Q_P value. This proportionality is evident from eqs (8) and (9), where the only difference is that t^* can be obtained by multiplying both sides of eq. (8) by $1/Q_P$, assuming a uniform Q_P.

For both t (Fig. 2e) and t^* (Fig. 2f), the absolute errors are smallest (equal to zero) along the principal axes (horizontal and vertical directions relative to the source) and largest along the diagonal directions. This can be attributed to the angle between wave front propagation and grid orientation, which is zero along the principal axes and reaches 45° in the diagonal directions. The larger the angle, the greater the errors introduced when solving eqs (8) and (9) using the FSM and MFSM with a rectangular mesh. Beyond the principal axes, the absolute errors in t and t^* accumulate with increasing distance from the source (Figs 2e and f). A similar phenomenon is observed in the grid-based fast marching method (FMM) when solving the traveltime field t (Alkhalifah & Fomel 2001). For both t (Fig. 2g) and t^* (Fig. 2h), the percentage errors are larger near the source and decrease significantly with distance. This occurs because, in Cartesian coordinates with a regular grid distribution, the wave front curvature near the source is high and undersampled, whereas further from the source, the wave front becomes flatter and is oversampled (e.g. Alkhalifah & Fomel 2001; Lan *et al.* 2012; Lan & Zhang 2013; Zhou *et al.* 2023). Close to the source (Figs 2g–h), the relative errors in t and t^* accumulates dramatically due to the singularity at the point source (e.g. Alkhalifah & Fomel 2001; Rawlinson & Sambridge 2004; Fomel *et al.* 2009). In the records of a horizontal receiver array, t and t^* calculated with different grid sizes show strong agreement with their analytical solutions (Figs 3a and b). To provide a clear comparison, Figs 3(c)–(f) show the absolute and relative errors of t and t^*, which gradually decrease with grid refinement. In Figs 3(e) and (f), the maximum relative error of both t and t^* decreases from ~ 10.8 ‰ (brown solid line) to ~ 1.08 ‰ (black solid line).

Although the uniform model is the simplest, it provides valuable insights into the fundamental characteristics of the $t^*(\boldsymbol{x})$ field. The accuracy of t^* is influenced by factors such as the angle between wave front propagation and grid orientation, the curvature of the wave front relative to the grid size, and the singularity at the point source.

3.2 Constant-gradient velocity and attenuation models

To further validate the MFSM for solving t^*, we consider Model 2, which incorporates a constant-gradient velocity (Fig. 4a), combined with an attenuation model that features either a uniform Q_P (Fig. 4b) or a constant-gradient Q_P (Fig. 4c). The region is initially partitioned with spatial intervals of $\Delta x = \Delta z = 0.20$ km, producing a grid of 151 by 151 points.

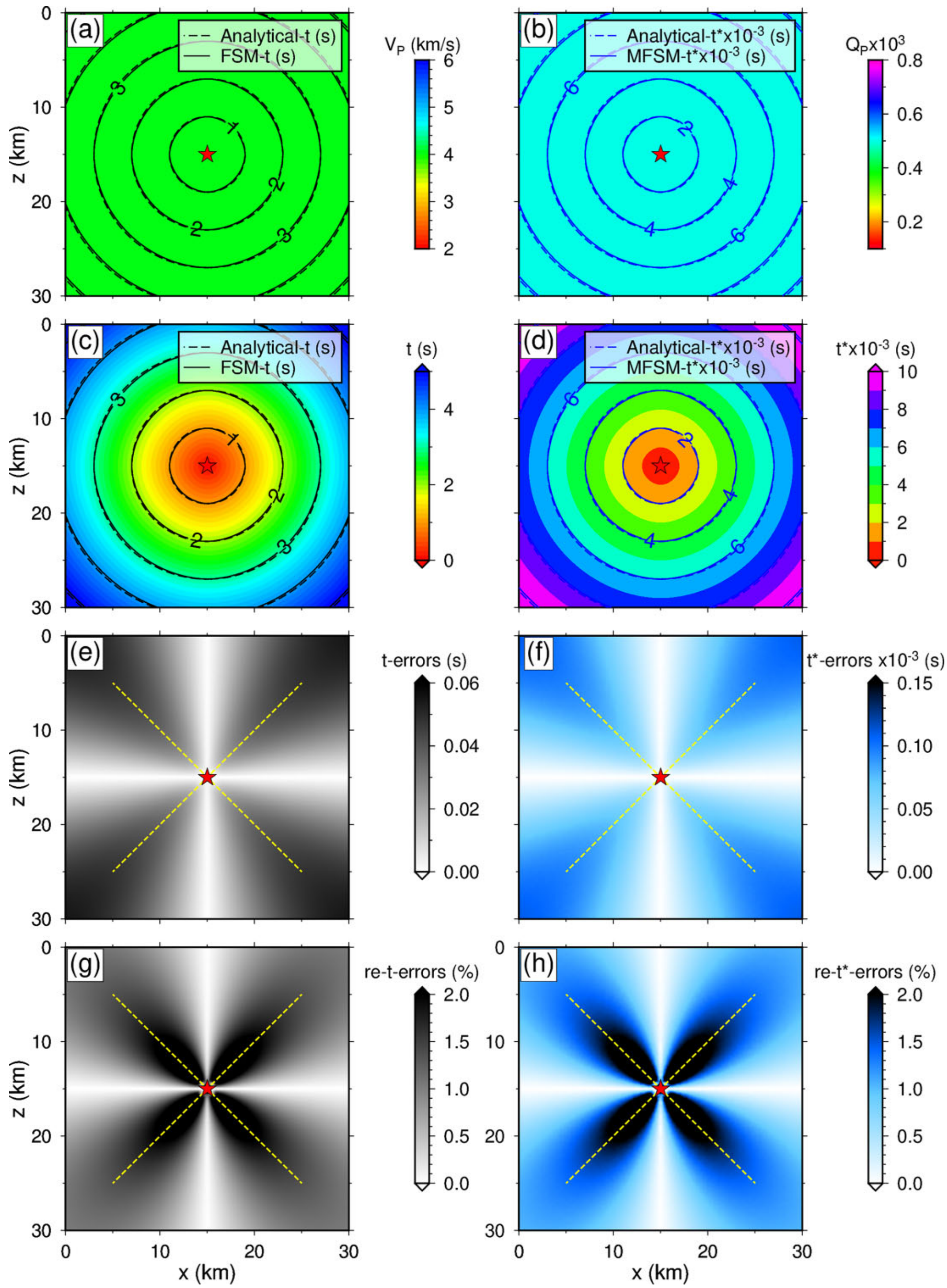

Figure 2. Model 1 consists of a uniform V_P (a) and a uniform Q_P (b), with V_P and Q_P specified as 4.0 km s^{-1} and 500.0, respectively. The source (red star) is located at (15 km, 15 km). Comparisons of isolines for $t(\boldsymbol{x})$ calculated using the FSM and the analytical solution are shown in (a) and (c), while those for $t^*(\boldsymbol{x})$ calculated using the MFSM and the analytical solution are shown in (b) and (d), respectively. The $t(\boldsymbol{x})$ and $t^*(\boldsymbol{x})$ fields are shown in (c) and (d), respectively. The absolute and relative (in percentage) errors for $t(\boldsymbol{x})$ are shown in (e) and (g), while the absolute and the relative (in percentage) errors for $t^*(\boldsymbol{x})$ are shown in (f) and (h). The yellow dashed lines along the diagonal directions represent auxiliary lines.

In Fig. 4(a), as V_P decreases from 6.0 to 2.0 km s^{-1} in z direction, $t(\boldsymbol{x})$ isolines become denser gradually. Adopting the uniform Q_P model, the t^* isolines (Fig. 4b) align with the t isolines (Fig. 4a), with their values maintaining a ratio of 1/500.0. However, when incorporating the constant-gradient Q_P model, the gradual decrease in Q_P in z direction leads to much denser t^* isolines (Fig. 4c). The analytical solution for $t(\boldsymbol{x})$ in a constant-gradient velocity model can be found in Fomel *et al.* (2009). For a uniform Q_P model

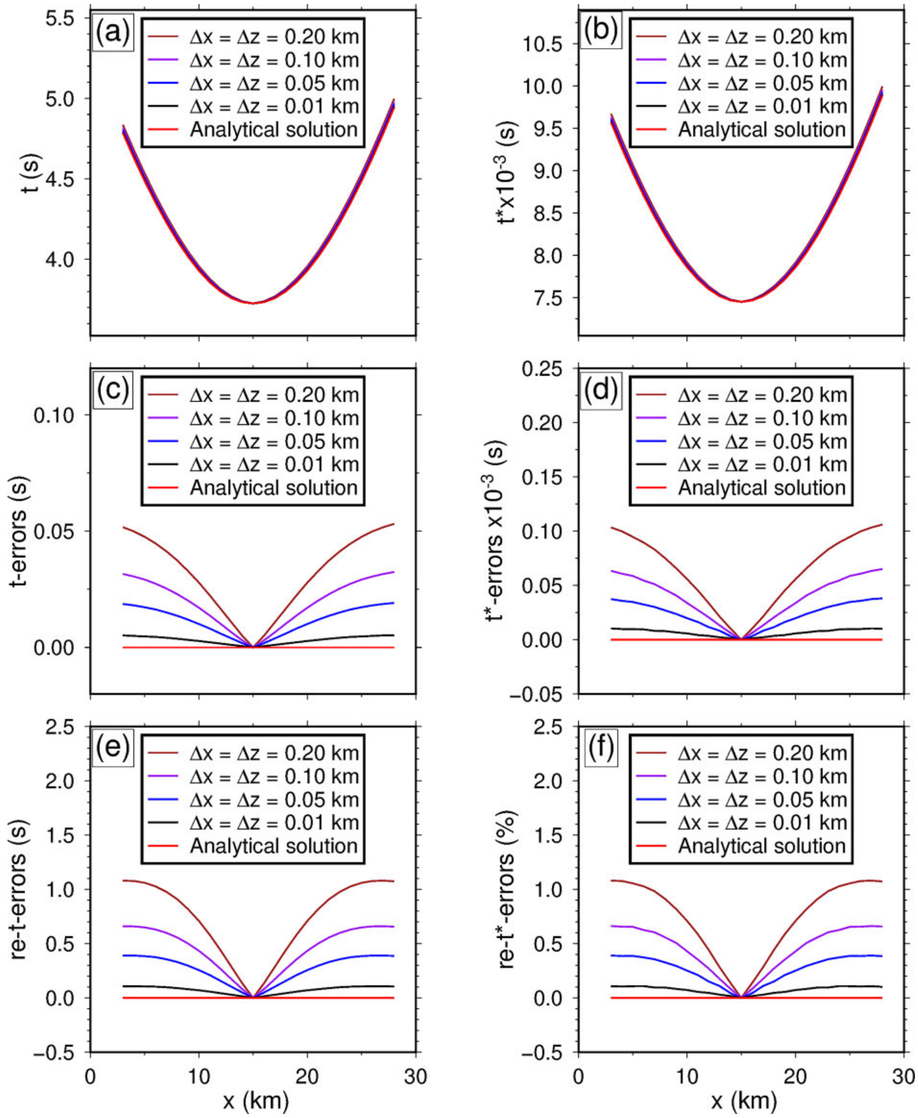

Figure 3. The recorded t and t^* for a horizontal receiver array spanning from (3 km, 0 km) to (28 km, 0 km) in Model 1 (Fig. 2). Compared to the analytical solution, t, along with the absolute and relative t errors (in percentage) calculated using the FSM with grid refinement are shown in (a), (c) and (e), respectively. Compared to the analytical solution, t^*, along with the absolute and relative t^* errors (in percentage) calculated using the MFSM with grid refinement are shown in (b), (d) and (f), respectively.

(Figs 4a and b), the derivation of the analytical solution for $t^*(\boldsymbol{x})$ is straightforward. When both V_P and Q_P have constant gradients (Figs 4a and c), we consider the numerical solution on a grid with 0.01 km spatial intervals to be accurate, as the grid spacing is sufficiently small to ensure precision. Therefore, the results calculated using this dense grid are taken as the reference solution. Alternatively, accurate $t^*(\boldsymbol{x})$ can also be computed by numerical integration along the analytical ray paths, which correspond to arcs of circles in a constant velocity gradient (Slotnick 1959). The $t(\boldsymbol{x})$ and $t^*(\boldsymbol{x})$ fields, along with their corresponding isolines, are shown in Figs 4(d)–(f).

In Figs 4(g), (h), (j) and (k), the absolute and relative errors of t and t^* directly above the source are non-zero, primarily due to the inexact first-order approximation of the derivatives of t with respect to z, as V_P gradually varies along the z direction. Another finding is that the largest absolute and relative errors for t and t^* (Figs 4g–h and j–k) progressively deviate from the diagonal directions as depth decreases. We attribute this deviation to the decrease in V_P with decreasing depth. As discussed in Section 3.1, the primary source of error stems from propagation distance inaccuracies caused by the angle between wave front propagation and grid orientation. Thus, in the constant-gradient velocity model (Fig. 4a), shallower depths with lower V_P result in larger t and t^* errors. For the uniform Q_P model (Fig. 4b), variations in the absolute and relative t^* errors result from changes in V_P and inaccuracies in t, with the latter also being influenced by variations in V_P. For the constant-gradient Q_P model (Fig. 4c), as Q_P decreases from 800.0 to 100.0, the absolute and relative t^* errors (Figs 4i and l) also deviate from the diagonal directions at shallower depths. This can be attributed to the fact that lower Q_P at shallower depths are more likely to generate larger t^* errors.

For the records of a horizontal receiver array, the absolute and relative errors in t and t^* systematically decrease as the grid is refined (Figs 5d–i). Specifically, for the uniform Q_P model (Fig. 4b), refining the grid size from 0.2 to 0.01 km reduces the maximum absolute t^* error from $\sim 0.144 \times 10^{-3}$ s (brown solid line) to $\sim$

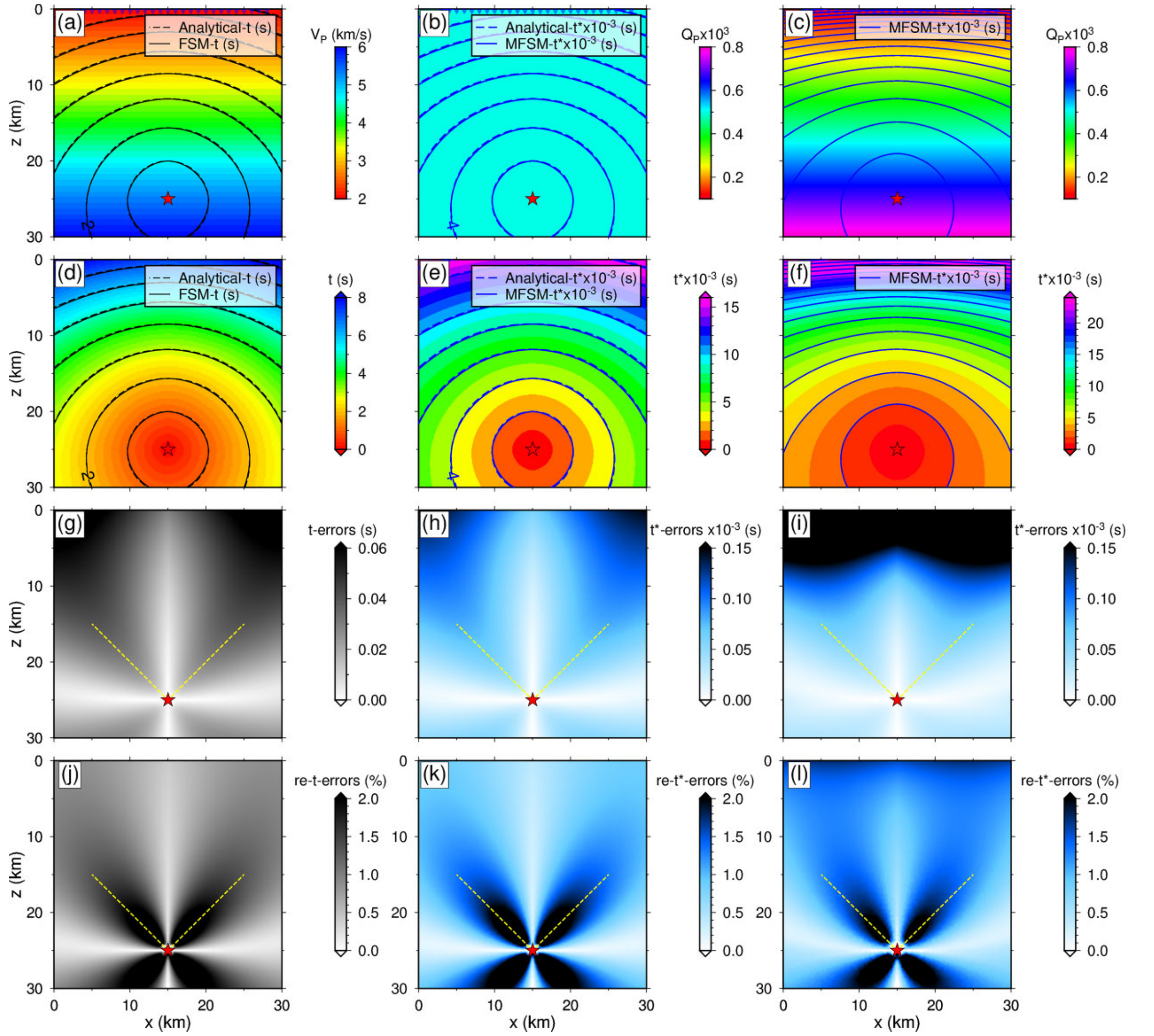

Figure 4. Model 2 consists of a constant-gradient V_P model (a) and a Q_P model that is either uniform (b) or has a constant-gradient (c). In (a), V_P is represented by $V_P(\boldsymbol{x}) = V_P(x, y, z) = 2.0 + \frac{30z}{6.0-2.0}$. In (b), Q_P is 500.0, while in (c), Q_P is represented by $Q_P(\boldsymbol{x}) = Q_P(x, y, z) = 100.0 + \frac{30z}{800.0-100.0}$. The red star represents the point source, while the blue inverted triangles in (a), (b) and (c) indicate a horizontal receiver array. Comparisons of isolines for $t(\boldsymbol{x})$ calculated using the FSM and the analytical solution are shown in (a) and (d), with the absolute and relative (in percentage) errors presented in (g) and (j), respectively. Including a uniform Q_P model (b), comparisons of isolines for $t^*(\boldsymbol{x})$ calculated using the MFSM and the analytical solution are shown in (b) and (e), with the absolute and relative (in percentage) errors presented in (h) and (k), respectively. Including a constant-gradient Q_P model (c), isolines for $t^*(\boldsymbol{x})$ calculated using the MFSM is shown in (c) and (f), while the absolute and relative (in percentage) errors between grid sizes of 0.20 km and 0.01 km are presented in (i) and (l), respectively. The yellow dashed lines along the diagonal directions represent auxiliary lines.

0.011×10^{-3} s (black solid line) (Fig. 5e). Similarly, the maximum relative t^* error decreases from ~ 8.8 ‰ (brown solid line) to ~ 0.7 ‰ (black solid line) in Fig. 5(h). For the constant-gradient Q_P model (Fig. 4c), as the grid size decreases from 0.2 to 0.01 km, the maximum absolute t^* error decreases by $\sim\ 0.518 \times 10^{-3}$ s (brown and black solid lines) (Fig. 5f), while the maximum relative t^* error decreases by ~ 1.77 % (brown and black solid lines) (Fig. 5i). At a grid size of 0.01 km (black solid line), the calculated results show negligible deviations from the analytical solutions (Figs 5e and h). Thus, we use the solutions calculated with this grid size as the reference for the constant-gradient V_P and constant-gradient Q_P model (Figs 5f and i).

Variations in V_P and/or Q_P influence the accumulation of t^* errors, with lower values of V_P and Q_P generally leading to larger errors. However, as the grid size is refined, these t^* errors progressively decrease and approach the analytical solution. These results demonstrate the effectiveness of the MFSM in accurately solving t^* in models with constant-gradient velocity and attenuation.

3.3 Heterogeneous velocity and attenuation models

In this section, we validate the MFSM for computing t^* in complex heterogeneous models with varying V_P and Q_P, both in Cartesian and spherical coordinates.

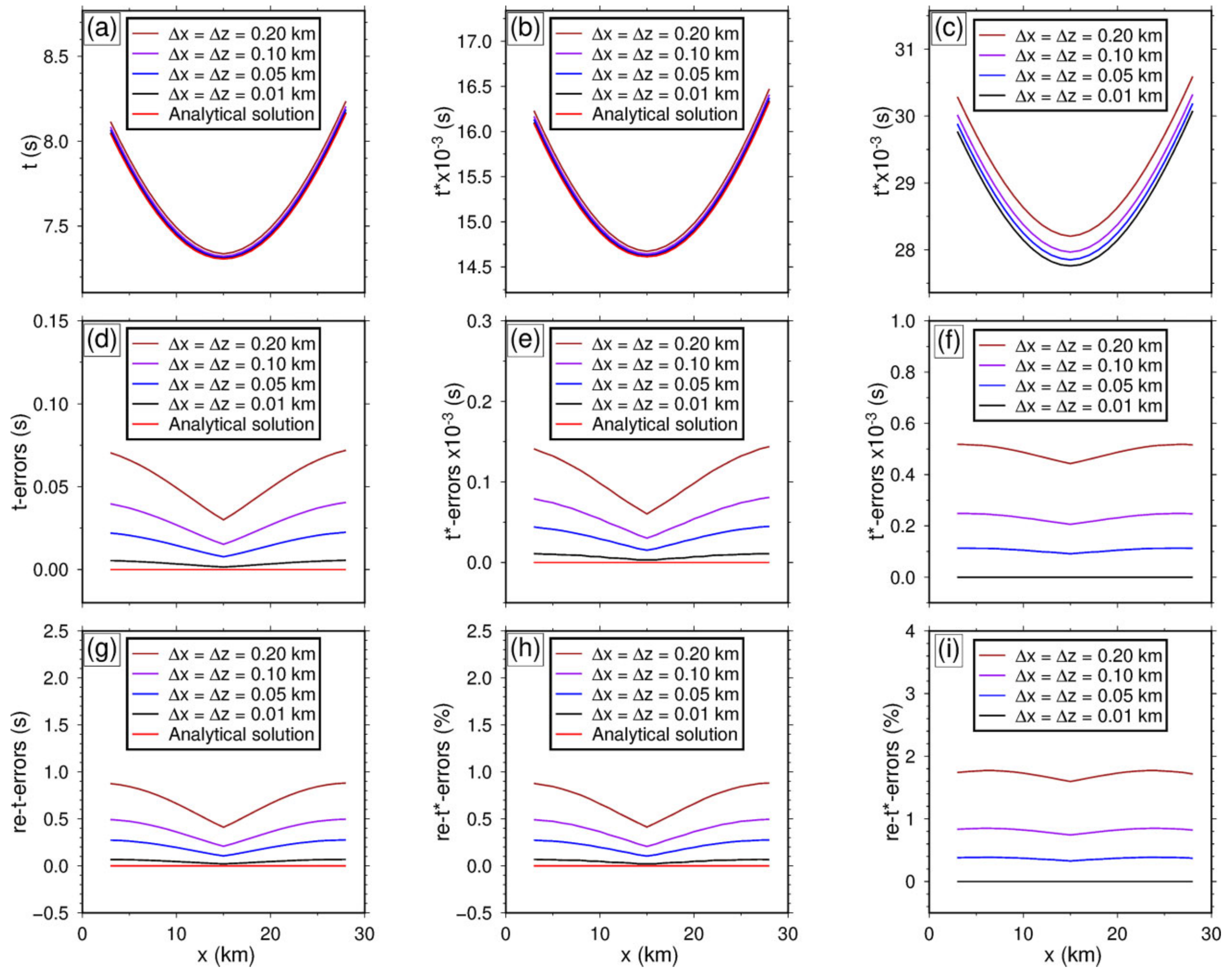

Figure 5. The recorded t and t^* for a horizontal receiver array spanning from (3 km, 0 km) to (28 km, 0 km) in Model 2 (Fig. 4). Compared to the analytical solution, t, along with the absolute and relative t errors (in percentage) calculated using the FSM with grid refinement are shown in (a), (d) and (g), respectively. Including the uniform Q_P model Figs 4(b), (e) and (h) show t^*, along with the absolute and relative t^* errors (in percentage) calculated using the MFSM with grid refinement and compared to the analytical solution. Including the constant-gradient Q_P model (Figs 4(c), (f) and (i) show t^*, along with the absolute and relative t^* errors (in percentage) calculated using the MFSM with grid refinement and compared to the solutions obtained using a dense grid of a spacing of 0.01 km.

3.3.1 Examples in Cartesian coordinates

We examine Model 3 in Cartesian coordinates, where the heterogeneous V_P model is randomly generated (Fig. 6a), superimposed with an attenuation model that is either a uniform ($Q_P = 500.0$, Fig. 6b) or randomly generated (Fig. 6c). The modelled region spans 30 km in the x direction and 15 km in the z direction. The source is placed at (15 km, 10 km). The region is discretized on grids with sizes $\Delta x = \Delta z$ of 0.09, 0.07, 0.05, 0.03 and 0.01 km, corresponding to grid resolutions of 335×168, 430×216, 601×301, 1001×501 and 3001×1501, respectively.

The high and low V_P and Q_P anomalies are randomly distributed across the region, thus the isolines of $t(\boldsymbol{x})$ and $t^*(\boldsymbol{x})$ exhibit heterogeneous patterns (Figs 6a–f). With a uniform Q_P model, the $t^*(\boldsymbol{x})$ field and its isolines (Figs 6b and e) closely resemble the patterns of the $t(\boldsymbol{x})$ field and its isolines (Figs 6a and d). However, when the random Q_P model is applied, the $t^*(\boldsymbol{x})$ field and its corresponding isolines (Figs 6c and f) become much more heterogeneous. The solutions computed using the finest grid size of 0.01 km are taken as the reference solution. The absolute errors in $t(\boldsymbol{x})$ and $t^*(\boldsymbol{x})$ for different grid sizes are illustrated in Figs 6(g)–(r). The patterns of these errors are closely linked to the distribution of the heterogeneous V_P and Q_P anomalies. Although the magnitudes of the $t(\boldsymbol{x})$ and $t^*(\boldsymbol{x})$ errors vary across the region, they systematically decrease as the grid size is refined from 0.09 to 0.01 km (Figs 6g–r).

3.3.2 Numerical examples in spherical coordinates

To broaden the method's applicability, we extend its application to compute t^* in spherical coordinates. The theoretical framework for this extension is detailed in Appendix A. For Model 4, the V_P and Q_P models are based on the AK135 reference model (Kennett *et al.* 1995), as shown in Figs 7(a) and (b). It should be noted that Q_P is determined by Q_μ and Q_κ, as no Q_P model is available in the Ak135 model. The V_P perturbation, depicted in Fig. 7(c), is derived from the MITP2008 model (Li *et al.* 2008), and represents the percentage deviation of V_P from the AK135 reference model. The Q_P perturbation, shown in Fig. 7(d), is obtained by scaling the V_P perturbation from Fig. 7(c). The source, marked by a black star, is positioned at a depth of 500.0 km.

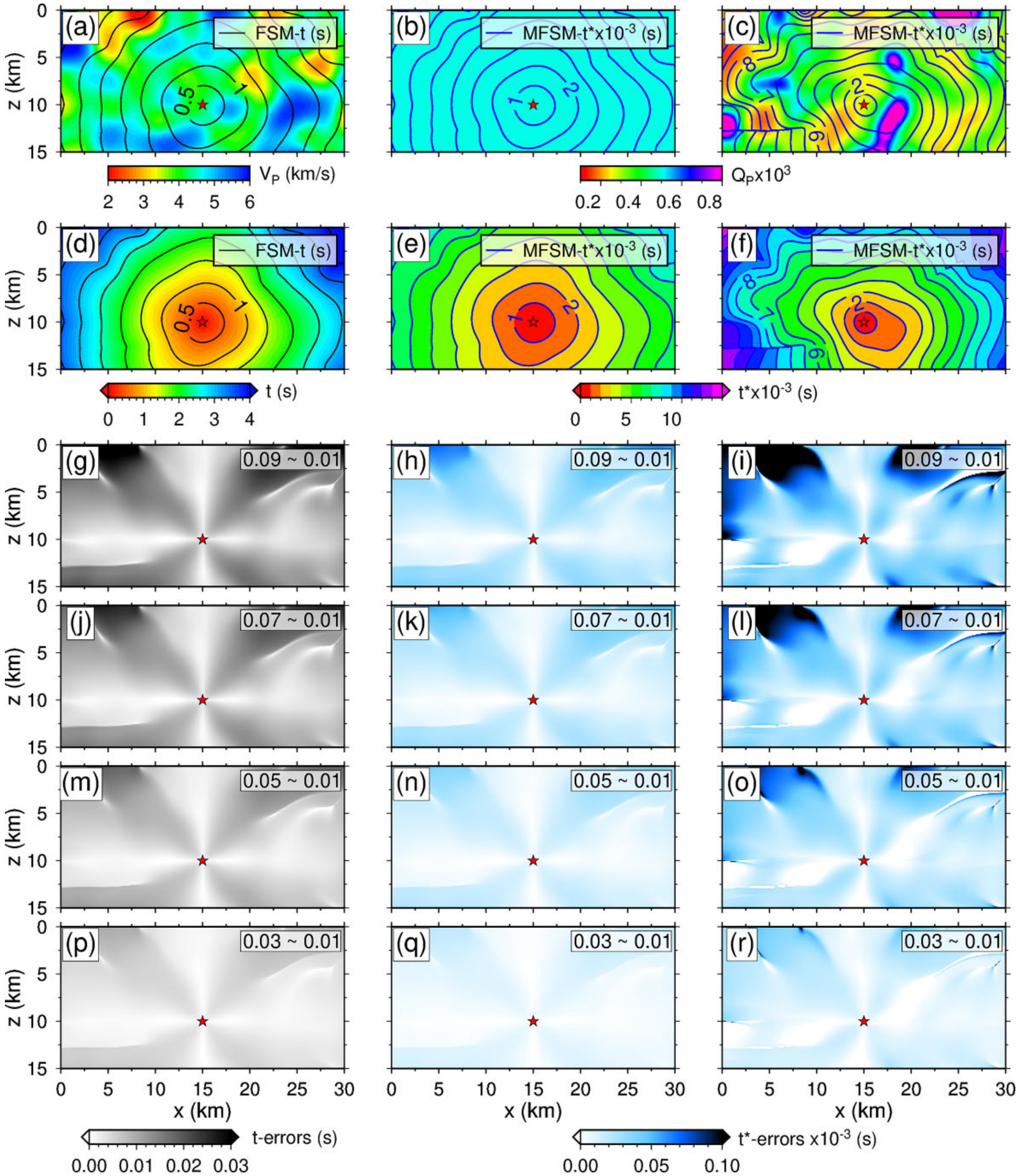

Figure 6. Model 3 consists of a heterogeneous V_P model (a) and a Q_P model that is either uniform (b) or heterogeneous (c). The source (red star) is positioned at (15 km, 10 km). Isolines for $t(\boldsymbol{x})$ (black solid lines) are shown in (a) and (d). Including the uniform Q_P model (b), isolines for $t^*(\boldsymbol{x})$ (blue solid lines) are shown in (b) and (e). Including the heterogeneous Q_P model (c), isolines for $t^*(\boldsymbol{x})$ (blue solid lines) are shown in (c) and (f). $t(\boldsymbol{x})$ and $t^*(\boldsymbol{x})$ fields are shown in (d), (e) and (f). With grid refinement from 0.09 to 0.01 km, (g), (j), (m) and (p) show the absolute $t(\boldsymbol{x})$ errors, and (h), (k), (n) and (q) show the absolute $t^*(\boldsymbol{x})$ errors for the uniform Q_P model, and (i), (l), (o) and (r) show the absolute $t^*(\boldsymbol{x})$ errors for the heterogeneous Q_P model. All errors are referenced against the dense grid of a size of 0.01 km.

With the grid size adjusted to $\Delta\phi = 0.004$, 0.003, 0.002 and 0.001 rad, and $\Delta r = 4.0$, 3.0, 2.0 and 1.0 km, the grid resolutions are 390×712, 520×949, 780×1424 and 1559×2847, respectively. It should be noted that, while the calculations are conducted in 3-D spherical coordinates (r, θ, ϕ), only three grid nodes are arranged in the θ-direction. The $t(\boldsymbol{x})$ and $t^*(\boldsymbol{x})$ fields, along with their isolines calculated using the FSM and MFSM, are shown in Figs 7(c)–(f). The absolute errors of $t(\boldsymbol{x})$ and $t^*(\boldsymbol{x})$ for varying grid sizes show a significant decrease with grid refinement (Figs 7g–l). We also present t and t^* records for a receiver array positioned at the surface, spanning from (45°, 0 km) to (135°, 0 km) in Fig. 8. The solutions for t and t^* calculated with the finest grid ($\Delta\phi = 0.001$ rad and $\Delta r = 1.0$ km) are used as reference solutions. As shown in Figs 8(c)–(f), both the absolute and relative errors of t and t^* decrease as the grid is refined. Specifically, as the grid size changes from $\Delta\phi = 0.004$ rad and $\Delta r = 4.0$ km to $\Delta\phi = 0.001$ rad and $\Delta r = 1.0$ km, the maximum absolute t^* errors decrease by 67.0×10^{-3} s (brown and black solid lines) (Fig. 8d), and the

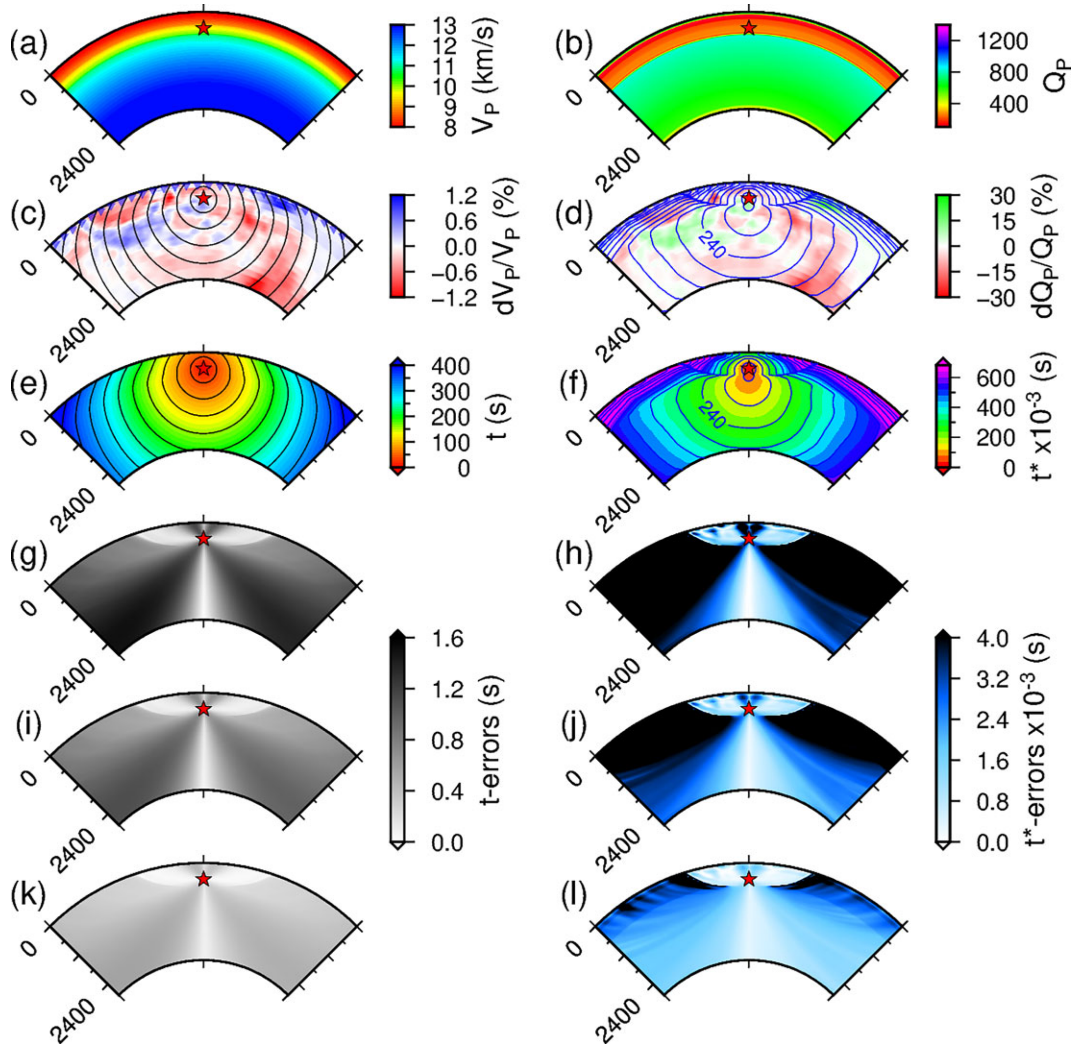

Figure 7. Model 4 consists of a V_P model showing the percent deviation (c) from the ak135 reference V_P model (a) and a Q_P model showing the percent deviation (d) from the Q_P model (b) derived from the ak135 reference. The source (red star) is positioned at 500.0 km depth. Isolines for $t(\boldsymbol{x})$ (black solid lines) are shown in (c) and (e), and isolines for $t^*(\boldsymbol{x})$ (blue solid lines) are shown in (d) and (f). $t(\boldsymbol{x})$ and $t^*(\boldsymbol{x})$ fields are illustrated in (e) and (f), respectively. The blue inverted triangles in (c) and (d) indicate the locations of a receiver array. With grid refinement from 0.004 rad and 4.0 km, 0.003 rad and 3.0 km to 0.002 rad and 2.0 km, the absolute $t(\boldsymbol{x})$ errors are shown in (g), (i) and (k), while the absolute $t^*(\boldsymbol{x})$ errors are shown in (h), (j) and (l). All errors are referenced to the dense grid of 0.001 rad and 1.0 km.

relative t^* errors decrease by 8.59 % (brown and black solid lines) (Fig. 8f).

These results, combined with those presented in Section 3.3.1, demonstrate that the MFSM is effective in solving for t^* in models with heterogeneous V_P and Q_P, in both Cartesian and spherical coordinates.

4 CONVERGENCE ANALYSIS, ITERATION COUNT AND COMPUTATIONAL TIME

We use Model 3 and Model 4 to quantitatively analyse the convergence behaviour, iteration count and computational time with grid refinement. The mean L^1 error for t^* over the entire region is calculated using the following formula:

$$L^1(t^*) = \frac{\sum_{i=1}^{M_I}\sum_{j=1}^{M_J}\sum_{k=1}^{M_K}\left|t^*_{\mathrm{ref},\,i,\,j,\,k} - t^*_{\mathrm{num},\,i,\,j,\,k}\right|}{M_I M_J M_K}, \tag{19}$$

where both t^*_{ref} and t_{num} are numerical solutions computed by the MFSM. Note that t^*_{ref} is the numerical solution computed with the finest mesh and t_{num} is the numerical solution computed with other mesh sizes. M_I, M_J and M_K, represent the number of grid points along the three coordinate axes, as introduced in Section 2.2. The order of accuracy for the n-th grid is calculated by

$$\mathrm{order} = \frac{\ln\frac{[L^1(t^*)]_n}{[L^1(t^*)]_{n-1}}}{\ln\frac{h_n}{h_{n-1}}}, \tag{20}$$

where $[L^1(t^*)]_n$ and h_n are the $L^1(t^*)$ error and grid spacing for the n-th grid, respectively.

For Model 3, the grid spacing, number of gridpoints, $L^1(t^*)$ error, order of accuracy and computing time for various mesh sizes are shown in Table 1. The reference solution is computed using a grid spacing of 0.01 km. As the grid spacing is refined from 0.10 to 0.02 km, the L^1 errors decreased significantly, from 3.999×10^{-5} to 0.599×10^{-5} s. We can observe that with grid refinement, the

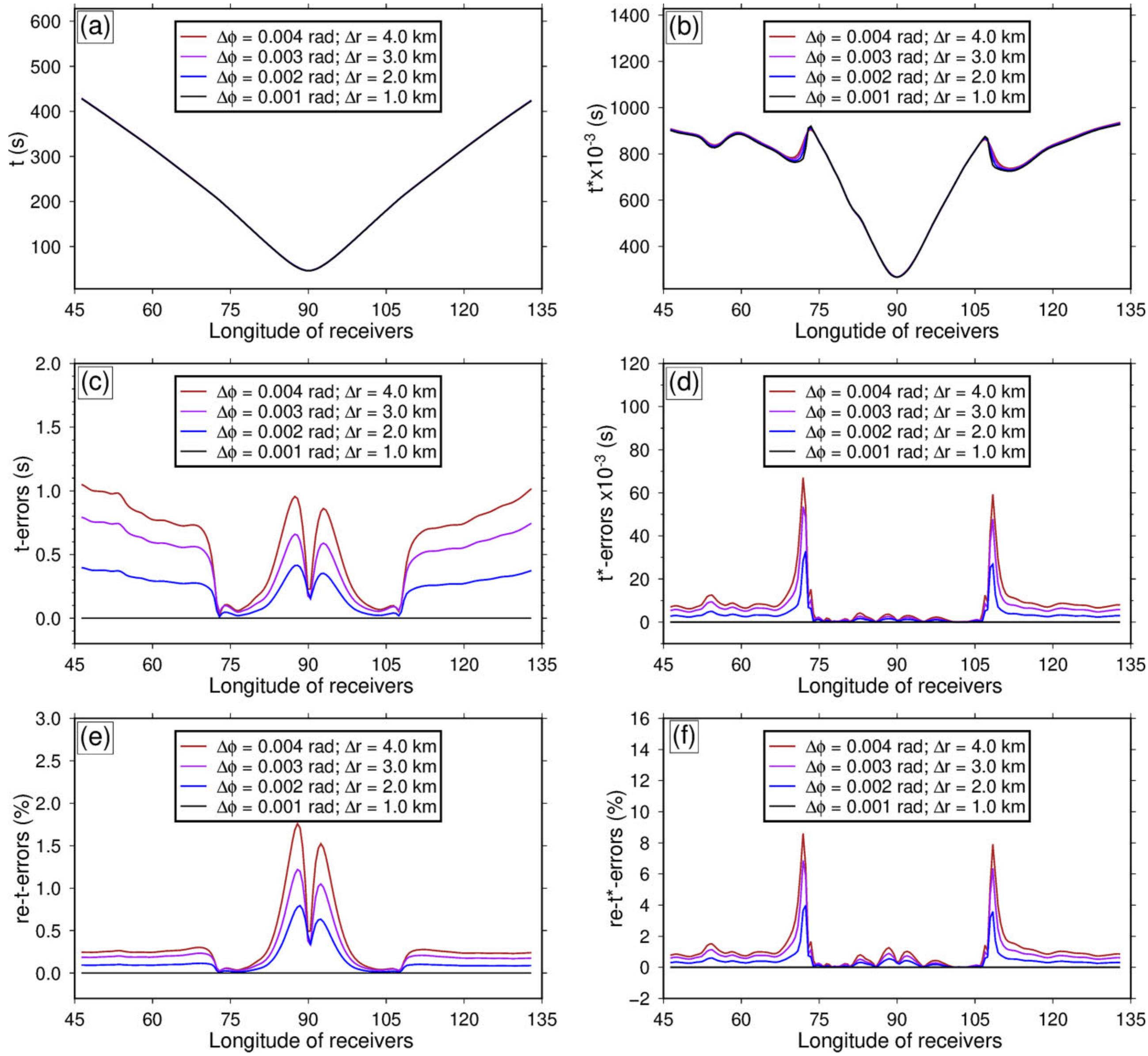

Figure 8. The recorded t and t^* for a horizontal receiver array in Model 4 (Fig. 7). The absolute and relative t errors (in percentage) calculated using the FSM with grid refinement are shown in (c) and (e), respectively. The absolute and relative t^* errors (in percentage) calculated using the MFSM with grid refinement are shown in (d) and (f), respectively. All errors are referenced to the dense grid of 0.001 rad and 1.0 km.

Table 1. Error analysis and computational efficiency of the MFSM for Model 3 in Cartesian coordinates.

Grid size (Δx; Δy; Δz)	Mesh	L^1 errors ($\times 10^{-5}$ s)	Order of accuracy	Time (s)	Iterations
0.10 km	301×151×3	3.999	–	0.516	3
0.09 km	335×168×3	3.536	1.170	0.526	3
0.08 km	376×189×3	3.212	0.816	0.779	3
0.07 km	430×216×3	2.873	0.835	0.980	3
0.06 km	501×251×3	2.470	0.979	1.305	3
0.05 km	601×301×3	2.051	1.019	2.010	3
0.04 km	751×376×3	1.583	1.161	3.069	3
0.03 km	1001×501×3	1.125	1.187	5.750	3
0.02 km	1501×751×3	0.599	1.556	15.062	3
0.01 km	3001×1501×3	–	–	74.111	3

Table 2. Error analysis and computational efficiency of the MFSM for Model 4 in spherical coordinates.

Grid size ($\Delta\phi$; $\Delta\theta$; Δr)	Mesh	L^1 errors ($\times 10^{-4}$ s)	Order of accuracy	Time (s)	Iterations
0.004 rad; 4.0 km	390×712×3	44.127	–	2.719	2
0.003 rad; 3.0 km	520×949×3	33.106	0.999	5.201	2
0.002 rad; 2.0 km	780×1424×3	17.636	1.553	12.078	2
0.001 rad; 1.0 km	1559×2847×3	–	–	64.011	2

MFSM achieves first-order accuracy and, in some cases, even higher accuracy (Table 1). The convergence criterion for calculating t^*, defined as the maximum difference between two consecutive iterations, is set to $\upsilon = 1.0 \times 10^{-12}$ s. For Model 3, only three Gauss–Seidel iterations are required to meet the convergence criterion. Similarly, for Model 4, Table 2 summarizes the grid spacing, number of gridpoints, $L^1(t^*)$ error, order of accuracy and computing time for different mesh sizes. The reference solution is computed using a grid spacing of $\Delta\phi = 0.001$ rad and $\Delta r = 1.0$ km. The L^1 errors decrease from 44.127×10^{-4} to 17.636×10^{-4} s as the grid is refined from $\Delta\phi = 0.004$ rad and $\Delta r = 4.0$ km to $\Delta\phi = 0.002$ rad and $\Delta r = 2.0$ km. The MFSM method can achieve precision exceeding first order when solving for t^* in spherical coordinates. Notably, only two Gauss–Seidel iterations are required to meet the convergence criterion. This analysis further manifests that the developed MFSM is accurate, efficient and exhibits robust convergence in calculating t^* in both Cartesian and spherical coordinates system.

5 APPLICATION IN NORTH ISLAND, NEW ZEALAND

In this section, we use the MFSM to solve for the t^* field based on the realistic V_P and Q_P models of the central North Island (Fig. 9a), and discuss the application of t^* in estimating earthquake response spectra.

The topographic map of the central North Island is shown in Fig. 9(a). The main tectonic and geological setting is as follows: In the central North Island, the Pacific and Australian plates are converging obliquely at a rate of 42 mm yr^{-1} (DeMets *et al.* 1994). This convergence is accommodated by the subduction of the Pacific plate and deformation of the overlying Australian plate. The North Island is situated above the Hikurangi subduction zone, which has resulted in volcanism and extension in the Taupō Volcanic Zone (TVZ). Volcanic activity within the TVZ varies along strike, with rhyolite-dominated caldera volcanoes in the central section and andesite-dominated cone volcanoes to the north and south (Fig. 9a).

The research region, outlined by the red solid line in the inset of Fig. 9(a), has an oblique shape. To reduce computational costs, the region is transformed into a regular grid with coordinates spanning $[-1.7^\circ,\ 2.0^\circ] \times [-3.0^\circ,\ 4.0^\circ]$. The 3-D V_P and Q_P models are extracted from the New Zealand Wide Model 2.2 (e.g. Eberhart-Phillips *et al.* 2010a, 2015) and interpolated onto a grid with dimensions of $160 \times 300 \times 160$. In Fig. 10, horizontal and vertical sections of the V_P and Q_P models passing through the source (red star) located at coordinates (175.88°, −38.72°, 100.0 km) are presented. The primary characteristics are as follows. The velocity model shows high V_P for the slab relative to the mantle wedge and reduced velocity for the mantle below the TVZ (Figs 10a–c). The Q_P model exhibits high Q_P $(900 - 1200)$ for the subducted cold slab and low Q_P (< 400) for the mantle wedge (Figs 10d–f). Significant variations are observed in the mantle wedge along the strike of the subduction zone, with the most pronounced low Q_P (< 250) occurring in the mantle wedge between depths of 50 and 85 km beneath the rhyolite-dominated, productive central segment of the TVZ (Figs 10e–f).

We consider three slab earthquakes at depths ranging from 50.0 to 200.0 km and calculate their corresponding t^* fields. As the slab earthquake depth is adjusted from 200.0 to 100.0 km and then to 50.0 km, it transitions from beneath the backarc, through the arc, to the forearc. As previously mentioned, t^* characterizes the spectral attenuation of earthquakes (magnitude ≥ 2.5) (Eberhart-Phillips & McVerry 2003) through $e^{-\omega t^*/2}$ (e.g. Cormier 1982; Bindi *et al.* 2006), which is routinely recorded by the seismographic network at the surface. Accordingly, t^* maps at a depth of 0 km for these three earthquakes are shown in Figs 9(b)–(d). For earthquakes at different depths, the corresponding t^* maps show distinct patterns (Figs 9b–d). For the earthquake beneath the backarc (Fig. 9b), a pronounced high t^* is observed at the TVZ, while a reduction in t^* appears southeast of the TVZ. For earthquakes beneath the arc and forearc, the high t^* region progressively shifts from southeast to northwest, with these regions showing progressively lower t^* (Figs 9c–d). Notably, in Figs 9(c) and (d), the TVZ consistently shows relatively high t^* compared to the surrounding regions. To explain these features, we present horizontal and vertical sections of the t and t^* fields for the earthquake beneath the arc in Fig. 10. Compared to t isolines shown in Figs 10(a)–(c) and (g)–(i), the t^* isolines are highly heterogeneous (Figs 10d–f and j–l). The low Q_P in the crust and mantle wedge beneath the TVZ compresses the t^* isolines, resulting in larger t^* (Fig. 9c). Conversely, the low t^* in the forearc region can mainly be attributed to wave propagation through the high Q_P slab.

The significant variations in V_P and Q_P across the North Island result in distinct t^* maps at the surface for earthquakes occurring at different depths (Figs 9b–d). These synthetic t^* values for various earthquakes can be converted into a path-averaged attenuation rate (CQ), which can then be used to refine the standard response spectral attenuation model (e.g. Eberhart-Phillips & McVerry 2003; Eberhart-Phillips *et al.* 2010b). To estimate CQ, it is usually necessary to calculate t^* for a range of source–receiver pairs. This is conventionally done by integrating along ray paths using $t^* = \int_L 1/(V(\boldsymbol{x})Q(\boldsymbol{x}))\mathrm{d}l$. However, as mentioned earlier, calculating t^* using this integration-based method can be time-consuming, especially when numerous source–receiver pairs are involved. As shown in Figs 9(b)–(d), the developed MFSM, which eliminates the need for ray tracing, provides a convenient to obtain t^*, thereby facilitating the estimation of earthquake response spectra.

6 DISCUSSION

The traditional FSM (Zhao 2005) is used to solve the eikonal and t^*-governing equations, but it does not account for the point source singularity, leading to inaccuracies near the source. Factored techniques (e.g. Fomel *et al.* 2009; Luo & Qian 2012; Luo *et al.* 2014) have been developed to address this issue by better approximating spherical wave fronts near the source. As a perspective for future work, one could improve the accuracy of t^* using the source factorization techniques.

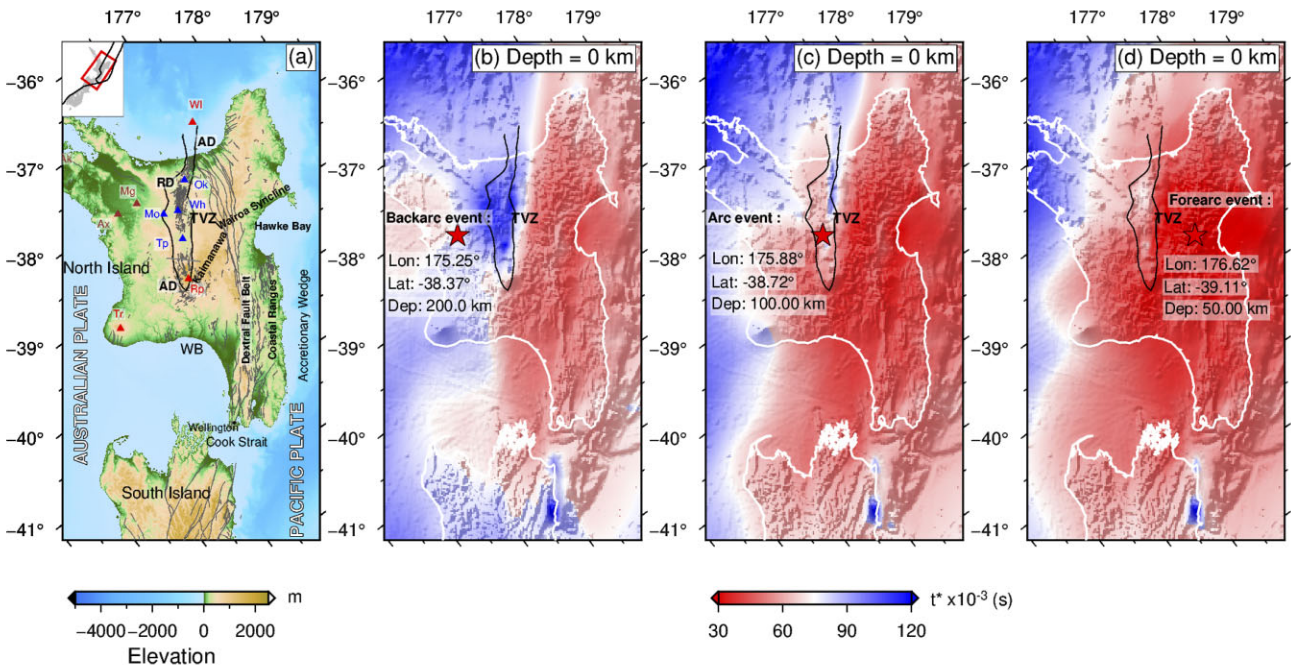

Figure 9. (a) Map of North Island, New Zealand, showing topography and major tectonic features. Major faults are indicated by grey lines. The research region is outlined by the red solid lines in the inset at the upper left corner, where the boundaries of the Australian Plate and the Pacific Plate are marked by black solid lines. The Taupō Volcanic Zone (TVZ) is marked by black solid curves. Volcanic features are marked as follows: calderas (blue triangles), active andesite volcanoes (red triangles) and non-silicic volcanic centres (brown triangles). Volcanic labels: Ak, Auckland; Ax, Alexandra; Mg, Maungataurari; WI, White Island; Ok, Okataina; Rp, Ruapehu; Tr, Taranaki; Mo, Mangakino; Wh, Whakamaru; Tp, Taupō. (b), (c) and (d) show surface t^* maps at 0 km depth, with slab earthquakes (red star) located beneath the backarc, arc and forearc regions, respectively.

The core of the developed MFSM is to compute $t^*(\boldsymbol{x})$ by solving its governing equation (eq. 9) based on the upwind approximation of the gradient $\nabla t(\boldsymbol{x})$, obtained from the numerical solution of the Eikonal equation (eq. 8), with the two equations solved in succession. Considering a formulation that is mathematically equivalent with eq. (9), fast-marching-like algorithms have been developed to solve it and typically require solving two governing equations simultaneously (e.g. Deschamps & Cohen 2001; Benmansour *et al.* 2010; Rouchdy & Cohen 2013; Peton & Lardjane 2022). This motivates the development of an alternative MFSM or a modified FMM that can solve $t(\boldsymbol{x})$ and $t^*(\boldsymbol{x})$ simultaneously. In addition, incorporating alternative methods like the fast iterative method (FIM) (e.g. Jeong & Whitaker 2008), finite-element method (FEM) (e.g. Pullan *et al.* 2002) or discontinuous Galerkin method (DGM) (e.g. Cheng & Shu 2007) into t^* solutions could expand forward modelling tools, particularly for adjoint-state attenuation tomography (e.g. He 2020; Huang *et al.* 2020).

At present, the FSM and MFSM are tested on a planar Earth's surface, but real-world applications often involve complex topography, such as mountainous or volcanic regions (e.g. Sun *et al.* 2011; García-Yeguas *et al.* 2012; Prudencio *et al.* 2015a, b). By integrating methods like unstructured grids (e.g. Rawlinson & Sambridge 2004; Qian *et al.* 2007) or the topography-dependent anisotropic eikonal equation (e.g. Lan & Zhang 2013; Mirebeau & Dreo 2017; Zhou *et al.* 2023), the MFSM could be adapted to effectively calculate t and t^* on irregular surfaces.

7 CONCLUSIONS

Seismic attenuation (mainly intrinsic and scattering attenuation) can cause changes in amplitude and phase for a propagating seismic wave, with these changes characterized by the attenuation operator t^*. Traditionally, t^* is calculated by integrating the reciprocal of the velocity-quality factor Q product along a ray path determined via ray tracing. To avoid ray tracing and enable the development of a ray-free attenuation tomography method, we propose a MFSM to directly compute t^*.

The MFSM computes t^* by numerically solving the differential form of its governing equation. First, the integral expressions for t and t^* are converted into differential forms using directional derivatives. By relating the directional derivative to the gradient, the eikonal equation for t and the governing equation for t^* are derived. The traveltime t is numerically computed using the classic fast sweeping method (Zhao 2005), and it remains fixed while solving for t^*. Given that t^* and t share the same ray path, the gradient of t^* (∇t^*) is discretized using the upwinding scheme derived from ∇t. The t^* field is then calculated by solving the discretized t^* governing equation using the Fast Sweeping Algorithm, based on the velocity and attenuation models, and the determined t field.

The developed MFSM is validated through several numerical experiments. First, t^* calculated by the MFSM is compared with analytical solutions for uniform and constant-gradient models, with an analysis of the absolute and relative t^* errors. For heterogeneous velocity and attenuation models, t^* cais lculated with grid refinement, and the convergence, iteration count and computation time of the MFSM are also evaluated. The effectiveness of the MFSM is demonstrated in both Cartesian and spherical coordinates. Finally, using a realistic velocity and attenuation model for North Island, New Zealand, we compute t^* field for different slab earthquakes and discuss the surface t^* and their role in estimating earthquake response spectra. In future work, this MFSM will be applied to develop an adjoint-state attenuation tomography method.

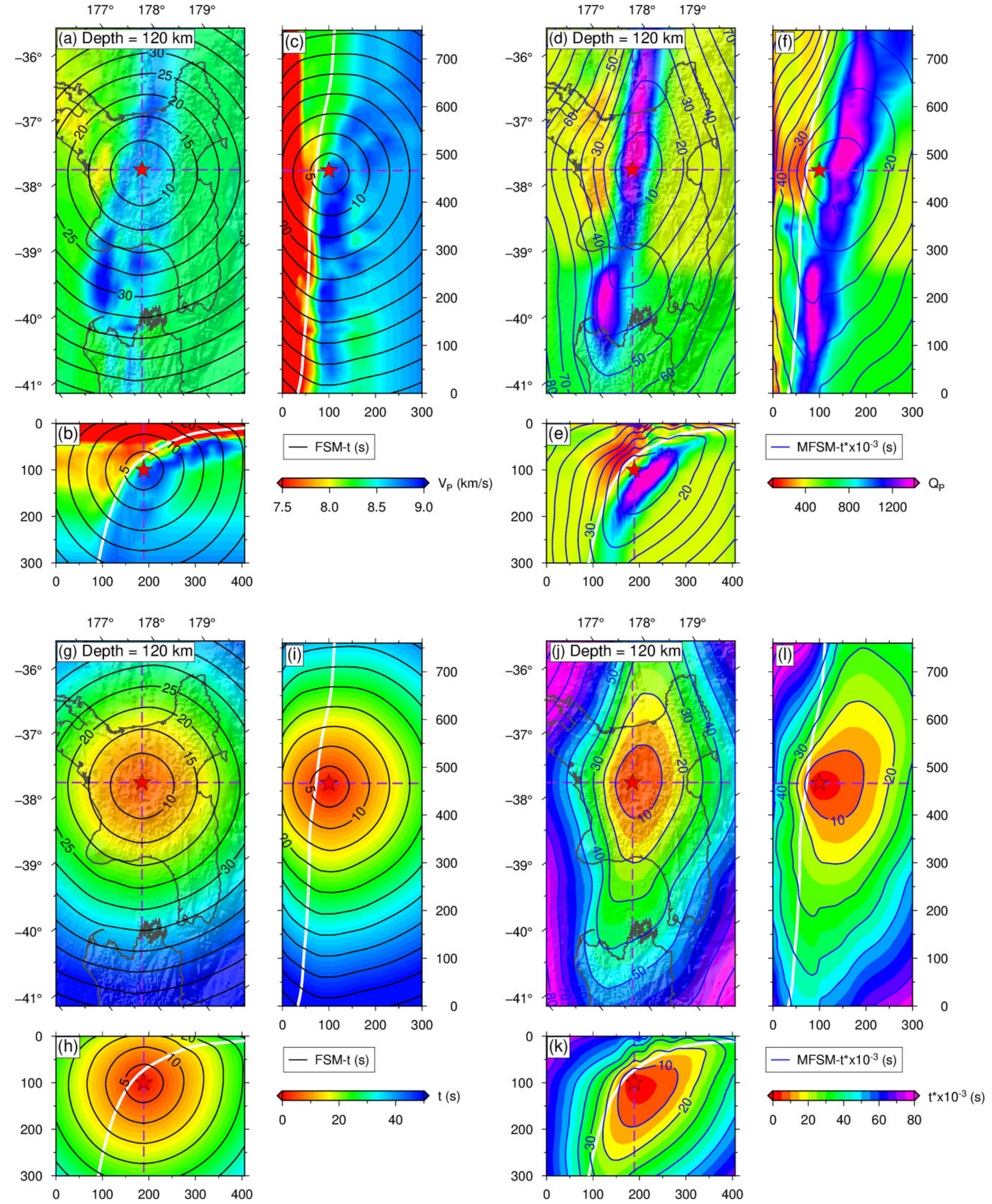

Figure 10. The horizontal and vertical sections passing through the source (red star) of the V_P (a–c) and Q_P (d–f) models, along with the $t(\boldsymbol{x})$ isolines (a–c), calculated using the FSM and $t^*(\boldsymbol{x})$ isolines (d–f), calculated by the MFSM. $t(\boldsymbol{x})$ and $t^*(\boldsymbol{x})$ fields, along with their isolines, are shown in panels (g)–(i) and (j)–(l), respectively. The earthquake, located beneath the arc region (Fig. 9b), has coordinates of 175.88° longitude, −38.72° latitude, and a depth of 100.0 km. The white solid lines in each vertical cross-section represent the location of the Slab 2.0 interface.

ACKNOWLEDGMENTS

We extend our gratitude to the Editor, Dr Ludovic Métivier and two anonymous reviewers for their valuable and constructive comments and suggestions. This study is funded by Ministry of Education, Singapore, under its MOE AcRF Tier-2 Grant (MOE-T2EP20122-0008).

DATA AVAILABILITY

All data produced in this work are available upon request via email at dongdong.wang@ntu.edu.sg. The velocity and attenuation model for the North New Zealand are publicly available from NZ-Wide2.2 (https://zenodo.org/records/3779523).

REFERENCES

Alkhalifah, T. & Fomel, S., 2001. Implementing the fast marching eikonal solver: spherical versus Cartesian coordinates, *Geophys. Prospect.,* **49,** 165–178.

Benmansour, F., Carlier, G., Peyré, G. & Santambrogio, F., 2010. Derivatives with respect to metrics and applications: subgradient marching algorithm, *Numer. Math.,* **116,** 357–381.

Bertrand, T., Makaroff, N. & Cohen, L. D., 2023. Fast marching energy CNN, in *International Conference on Scale Space and Variational Methods in Computer Vision,* pp. 276–287, eds Calatroni, L., Donatelli, M., Morigi, S., Prato, M. & Santacesaria, M., Springer.

Block, L. V., 1991. *Joint Hypocenter-Velocity Inversion of Local Earthquake Arrival Time Data in Two Geothermal Regions,* Doctoral dissertation, Massachusetts Institute of Technology.

Bindi, D., Parolai, S., Grosser, H., Milkereit, C. & Zunbul, S., 2006. Cumulative attenuation along source-to-receiver paths in northwestern Turkey, *Bull. seism. Soc. Am.,* **96,** 188–199.

Červený, V., 1987. Ray tracing algorithms in three-dimensional laterally varying layered structures, in *Seismic Tomography: With Applications in Global Seismology and Exploration Geophysics,* pp. 99–133, Springer Netherlands, Dordrecht.

Červený, V., 2010. *Seismic Ray Theory,* Cambridge Univ. Press.

Cohen, L. D. & Kimmel, R., 1997. Global minimum for active contour models: a minimal path approach, *Int. J. Comput. Vision.,* **24,** 57–78.

Cohen, L. D., 2006. Minimal paths and fast marching methods for image analysis, in *Handbook of Mathematical Models in Computer Vision,* pp. 97–111, Springer US.

Cheng, Y. & Shu, C. W., 2007. A discontinuous Galerkin finite element method for directly solving the Hamilton–Jacobi equations, *J. Comput. Phys.,* **223,** 398–415.

Cormier, V. F., 1982. The effect of attenuation on seismic body waves, *Bull. seism. Soc. Am.,* **72,** S169–S200.

Deschamps, T. & Cohen, L. D., 2001. Fast extraction of minimal paths in 3D images and applications to virtual endoscopy, *Med. Image. Anal.,* **5,** 281–299.

De Siena, L., Del Pezzo, E., Bianco, F. & Tramelli, A., 2009. Multiple resolution seismic attenuation imaging at Mt. Vesuvius, *Phys. Earth planet. Inter.,* **172,** 17–32.

De Siena, L., Del Pezzo, E. & Bianco, F., 2010. Seismic attenuation imaging of Campi Flegrei: Evidence of gas reservoirs, hydrothermal basins, and feeding systems, *J. geophys. Res.,* **115**. doi:10.1029/2009JB006938.

De Siena, L., Thomas, C., Waite, G. P., Moran, S. C. & Klemme, S., 2014. Attenuation and scattering tomography of the deep plumbing system of Mount St. Helens, *J. geophys. Res.,* **119,** 8223–8238.

DeMets, C., Gordon, R. G., Argus, D. F. & Stein, S., 1994. Effect of recent revisions to the geomagnetic reversal time scale on estimates of current plate motions, *Geophys. Res. Lett.,* **21,** 2191–2194.

Eberhart-Phillips, D. & McVerry, G., 2003. Estimating slab earthquake response spectra from a 3D Q model, *Bull. seism. Soc. Am.,* **93,** 2649–2663.

Eberhart-Phillips, D., Reyners, M., Chadwick, M. & Stuart, G., 2008. Three-dimensional attenuation structure of the Hikurangi subduction zone in the central North Island, New Zealand, *Geophys. J. Int.,* **174,** 418–434.

Eberhart-Phillips, D., Reyners, M., Bannister, S., Chadwick, M. & Ellis, S., 2010. Establishing a versatile 3-D seismic velocity model for New Zealand, *Seismol. Res. Lett.,* **81,** 992–1000.

Eberhart-Phillips, D., McVerry, G. & Reyners, M., 2010. Influence of the 3D distribution of Q and crustal structure on ground motions from the 2003 Mw 7.2 Fiordland, New Zealand, earthquake, *Bull. seism. Soc. Am.,* **100,** 1225–1240.

Eberhart-Phillips, D., Reyners, M. & Bannister, S., 2015. A 3D QP attenuation model for all of New Zealand, *Seismol. Res. Lett.,* **86,** 1655–1663.

Fomel, S., Luo, S. & Zhao, H., 2009. Fast sweeping method for the factored eikonal equation, *J. Comput. Phys.,* **228,** 6440–6455.

García-Yeguas, A., Koulakov, I., Ibáñez, J. M. & Rietbrock, A., 2012. High resolution 3D *P* wave velocity structure beneath Tenerife Island (Canary Islands, Spain) based on tomographic inversion of active-source data, *J. geophys. Res.,* **117,** doi:10.1029/2011JB008970.

He, Y., Han, S. & Luo, Y., 2020. Tomographic Q inversion based on the adjoint-state method, in *EAGE 2020 Annual Conference & Exhibition Online,* European Association of Geoscientists & Engineers. **Vol. 2020,** pp. 1–5

He, Y., 2022. Parallel fast sweeping method for computing seismic attenuated time, in *83rd EAGE Annual Conference & Exhibition,* European Association of Geoscientists & Engineers.**Vol. 2022,** pp. 1–5

Huang, X., Guo, Z., Zhou, H. & Yue, Y., 2020. First arrival Q tomography based on an adjoint-state method, *J. Geophys. Eng.,* **17,** 577–591.

Julian, B. R. & Gubbins, D., 1977. Three-dimensional seismic ray tracing, *J. Geophys.,* **43,** 95–113.

Jeong, W. K. & Whitaker, R. T., 2008. A fast iterative method for eikonal equations, *SIAM J. Sci. Comput.,* **30,** 2512–2534.

Kanamori, H., 1967. Spectrum of short-period core phases in relation to the attenuation in the mantl, *J. geophys. Res.,* **72,** 2181–2186.

Kennett, B. L., Engdahl, E. R. & Buland, R., 1995. Constraints on seismic velocities in the Earth from traveltimes, *Geophys. J. Int.,* **122,** 108–124.

Keers, H., Vasco, D. W. & Johnson, L. R., 2001. Viscoacoustic crosswell imaging using asymptotic waveforms, *Geophysics.,* **66,** 861–870.

Lan, H. Q., Zhang, Z., Xu, T., Bai, Z. M. & Liang, K., 2012. A comparative study on the fast marching and fast sweeping methods in the calculation of first-arrival traveltime field, *Progr. Geophys.,* **27,** 1863–1870.

Lan, H. & Zhang, Z., 2013. Topography-dependent eikonal equation and its solver for calculating first-arrival traveltimes with an irregular surface, *Geophys. J. Int.,* **193,** 1010–1026.

Lees, J. M. & Lindley, G. T., 1994. Three-dimensional attenuation tomography at Loma Prieta: Inversion of t∗ for Q, *J. geophys. Res.,* **99,** 6843–6863.

Leung, S. & Qian, J., 2006. An adjoint state method for three-dimensional transmission traveltime tomography using first-arrivals, *Commun. Math. Sci.,* **4**

Li, C., van der Hilst, R. D., Engdahl, E. R. & Burdick, S., 2008. A new global model for P wave speed variations in Earth's mantle, *Geochem. Geophys. Geosyst.,* **9**.

Luo, S. & Qian, J., 2012. Fast sweeping methods for factored anisotropic eikonal equations: multiplicative and additive factors, *J. Sci. Comput.,* **52,** 360–382.

Luo, S., Qian, J. & Burridge, R., 2014. High-order factorization based high-order hybrid fast sweeping methods for point-source eikonal equations, *SIAM. J. Numer. Anal.,* **52,** 23–44.

Mirebeau, J. M. & Dreo, J., 2017. Automatic differentiation of non-holonomic fast marching for computing most threatening trajectories under sensors surveillance, in *International Conference on Geometric Science of Information,* pp. 791–800, eds Nielsen, F. & Barbaresco, F., Springer.

Peton, N. & Lardjane, N., 2022. An Eulerian version of geometrical blast dynamics for 3D simulations, *Shock Waves.,* **32,** 241–259.

Prudencio, J., De Siena, L., Ibáñez, J. M., Del Pezzo, E., Garcia-Yeguas, A. & Diaz-Moreno, A., 2015. The 3D attenuation structure of deception Island (Antarctica), *Surv. Geophys.,* **36,** 371–390.

Prudencio, J., Ibáñez, J. M., Del Pezzo, E., Martí, J., García-Yeguas, A. & De Siena, L., 2015b. 3D attenuation tomography of the volcanic island of Tenerife (Canary Islands), *Surv. Geophys.,* **36,** 693–716.

Pullan, A. J., Tomlinson, K. A. & Hunter, P. J., 2002. A finite element method for an eikonal equation model of myocardial excitation wavefront propagation, *SIAM J. Appl. Math.,* **63,** 324–350.

Qian, J., Zhang, Y. T. & Zhao, H. K., 2007. Fast sweeping methods for eikonal equations on triangular meshes, *SIAM J. Numer. Anal.,* **45,** 83–107.

Rawlinson, N., Houseman, G. A. & Collins, C. D., 2001. Inversion of seismic refraction and wide-angle reflection traveltimes for three-dimensional layered crustal structure, *Geophys. J. Int.,* **145,** 381–400.

Rawlinson, N. & Sambridge, M., 2004. Wave front evolution in strongly heterogeneous layered media using the fast marching method, *Geophys. J. Int.,* **156,** 631–647.

Rawlinson, N., Pozgay, S. & Fishwick, S., 2010. Seismic tomography: a window into deep Earth, *Phys. Earth planet. Inter.,* **178,** 101–135.

Rouchdy, Y. & Cohen, L. D., 2013. Geodesic voting for the automatic extraction of tree structures. Methods and applications, *Comput. Vis. Image Underst.,* **117,** 1453–1467.

Sato, H., Fehler, M. C. & Maeda, T., 2012. *Seismic Wave Propagation and Scattering in the Heterogeneous Earth (Vol. 496),* Springer.

Sambridge, M. S., 1990. Non-linear arrival time inversion: constraining velocity anomalies by seeking smooth models in 3-D, *Geophys. J. Int.,* **102,** 653–677.

Sethian, J. A. & Popovici, A. M., 1999. 3-D traveltime computation using the fast marching method, *Geophysics.,* **64,** 516–523.

Sethian, J. A., 1996. A fast marching level set method for monotonically advancing fronts, *Proc. Nat. Acad. Sci.,* **93,** 1591–1595.

Shearer, P. M., 2019. *Introduction to Seismology,* Cambridge Univ. Press.

Sketsiou, P., De Siena, L., Gabrielli, S. & Napolitano, F., 2021. 3-D attenuation image of fluid storage and tectonic interactions across the Pollino fault network, *Geophys. J. Int.,* **226,** 536–547.

Slotnick, M. M., 1959. *Lessons in Seismic Computing,* SEG.

Stachnik, J. C., Abers, G. A. & Christensen, D. H., 2004. Seismic attenuation and mantle wedge temperatures in the Alaska subduction zone, *J. geophys. Res.,* **109**. doi:10.1029/2004JB003018.

Sun, J., Sun, Z. & Han, F., 2011. A finite difference scheme for solving the eikonal equation including surface topography, *Geophysics.,* **76,** T53–T63.

Um, J. & Thurber, C., 1987. A fast algorithm for two-point seismic ray tracing, *Bull. seism. Soc. Am.,* **77,** 972–986.

Wei, S. S. & Wiens, D. A., 2018. *P*-wave attenuation structure of the Lau back-arc basin and implications for mantle wedge processes, *Earth. planet. Sci. Lett.,* **502,** 187–199.

Zhao, H., 2005. A fast sweeping method for eikonal equations, *Math. Comput.,* **74,** 603–627.

Zhou, X., Lan, H., Chen, L., Guo, G., Bin Waheed, U. & Badal, J., 2023. A topography-dependent eikonal solver for accurate and efficient computation of traveltimes and their derivatives in 3D heterogeneous media, *Geophysics,* **88,** U17–U29.

APPENDIX A: THE CALCULATION OF TRAVELTIME t AND ATTENUATION OPERATOR t^* IN SPHERICAL COORDINATES

To address the specific application scenario for the earthquake tomography, we present the algorithm for solving eqs (8) and (9) in spherical coordinates $\boldsymbol{x} = (r, \theta, \phi)$. r represents the distance to the Earth's centre. θ and ϕ respectively denote the latitude and longitude. The gradient of $t(\boldsymbol{x})$ is $\nabla t(\boldsymbol{x}) = (\partial_r t, \frac{1}{r}\partial_\theta t, \frac{1}{r\cos\theta}\partial_\phi t)$. Ω represents the Earth's volume in the 3-D space $\mathcal{R} \times \Theta \times \Phi = [0, \infty) \times [-\frac{1}{2}\pi, \frac{1}{2}\pi] \times [0, 2\pi)$. In spherical coordinates, the computational domain Ω is partitioned into a uniform mesh with grid points $\boldsymbol{x}_{i,j,k}$ and mesh sizes Δr, $\Delta\theta$ and $\Delta\phi$. The total number of the grid points in three directions are M_I, M_J and M_K, respectively. Employing the Godunov upwind difference scheme to discretize eq. (8) at interior grid points ($2 \le i \le M_I - 1, 2 \le j \le M_J - 1, 2 \le k \le M_K - 1$):

$$\left[\frac{(t_{i,j,k} - t_{i,j,k}^{r\,\min})^+}{\Delta r}\right]^2 + \left[\frac{(t_{i,j,k} - t_{i,j,k}^{\theta\,\min})^+}{r_{i,j,k}\Delta\theta}\right]^2 + \left[\frac{(t_{i,j,k} - t_{i,j,k}^{\phi\,\min})^+}{r_{i,j,k}\cos\theta_{i,j,k}\Delta\phi}\right]^2 = s_{i,j,k}^2, \tag{A1}$$

where

$$t_{i,j,k}^{r\,\min} = \min(t_{i-1,j,k}, t_{i+1,j,k}),\ t_{i,j,k}^{\theta\,\min} = \min(t_{i,j-1,k}, t_{i,j+1,k}),\ t_{i,j,k}^{\phi\,\min} = \min(t_{i,j,k-1}, t_{i,j,k+1}) \tag{A2}$$

and

$$(x)^+ = \begin{cases} x, & x > 0, \\ 0, & x \le 0. \end{cases} \tag{A3}$$

At the boundary of the domain (i.e., $i = 1 \vee M_I; j = 1 \vee M_J; k = 1 \vee M_K$), the one-sided differences are used. For example, at the upper boundary $\boldsymbol{x}_{1,j,k}$, we have

$$\left[\frac{(t_{1,j,k} - t_{2,j,k})^+}{\Delta r}\right]^2 + \left[\frac{(t_{1,j,k} - t_{i,j,k}^{\theta\,\min})^+}{r_{i,j,k}\Delta\theta}\right]^2 + \left[\frac{(t_{1,j,k} - t_{i,j,k}^{\phi\,\min})^+}{r_{i,j,k}\cos\theta_{i,j,k}\Delta\phi}\right]^2 = s_{i,j,k}^2. \tag{A4}$$

Similar to that used in the Cartesian coordinates, we then employ the Fast Sweeping Algorithm to solve eqs (A1) and (A4).

In spherical coordinates, t^* governing eq. (9) can be written in the following form,

$$\begin{aligned} &\frac{\left(t_{i,j,k} - t_{i,j,k}^{r\,\min}\right)^+}{\Delta r}\frac{\left(t^*_{i,j,k} - t_{i,j,k}^{*,r\,\min}\right)}{\Delta r} + \frac{\left(t_{i,j,k} - t_{i,j,k}^{\theta\,\min}\right)^+}{r_{i,j,k}\Delta\theta}\frac{\left(t^*_{i,j,k} - t_{i,j,k}^{*,\theta\,\min}\right)}{r_{i,j,k}\Delta\theta} + \\ &\frac{\left(t_{i,j,k} - t_{i,j,k}^{\phi\,\min}\right)^+}{r_{i,j,k}\cos\theta_{i,j,k}\Delta\phi}\frac{\left(t^*_{i,j,k} - t_{i,j,k}^{*,\phi\,\min}\right)}{r_{i,j,k}\cos\theta_{i,j,k}\Delta\phi} = s_{i,j,k}^2 q_{i,j,k}, \end{aligned} \tag{A5}$$

where $t_{i,j,k}^{*,r\,\min}$, $t_{i,j,k}^{*,\theta\,\min}$ and $t_{i,j,k}^{*,\phi\,\min}$ can be determined by:

$$t_{i,j,k}^{*,r\,\min} = \begin{cases} t^*_{i-1,j,k}, & \text{if } t_{i,j,k}^{r\,\min} = t_{i-1,j,k}, \\ t^*_{i+1,j,k}, & \text{if } t_{i,j,k}^{r\,\min} = t_{i+1,j,k}, \end{cases} \tag{A6}$$

$$t_{i,j,k}^{*,\theta\,\min} = \begin{cases} t^*_{i,j-1,k}, & \text{if } t_{i,j,k}^{\theta\,\min} = t_{i,j-1,k}, \\ t^*_{i,j+1,k}, & \text{if } t_{i,j,k}^{\theta\,\min} = t_{i,j+1,k}, \end{cases} \tag{A7}$$

$$t_{i,j,k}^{*,\phi\,\min} = \begin{cases} t^*_{i,j,k-1}, & \text{if } t_{i,j,k}^{\phi\,\min} = t_{i,j,k-1}, \\ t^*_{i,j,k+1}, & \text{if } t_{i,j,k}^{\phi\,\min} = t_{i,j,k+1}. \end{cases} \tag{A8}$$

While employing one-sided differences at the boundary of the computational region, the difference form at the upper boundary, for example, will be

$$\begin{aligned} &\frac{\left(t_{1,j,k} - t_{2,j,k}\right)^+}{\Delta r}\frac{\left(t^*_{1,j,k} - t^*_{2,j,k}\right)}{\Delta r} + \frac{\left(t_{1,j,k} - t_{i,j,k}^{\theta\,\min}\right)^+}{r_{i,j,k}\Delta\theta}\frac{\left(t^*_{1,j,k} - t_{i,j,k}^{*,\theta\,\min}\right)}{r_{i,j,k}\Delta\theta} + \\ &\frac{\left(t_{1,j,k} - t_{i,j,k}^{\phi\,\min}\right)^+}{r_{i,j,k}\cos\theta_{i,j,k}\Delta\phi}\frac{\left(t^*_{1,j,k} - t_{i,j,k}^{*,\phi\,\min}\right)}{r_{i,j,k}\cos\theta_{i,j,k}\Delta\phi} = s_{i,j,k}^2 q_{i,j,k}, \end{aligned} \tag{A9}$$

Finally, we use the Fast Sweeping Algorithm to solve eqs (A5) and (A9).